Low Temperature Ethanol Steam Reforming for process intensification: new Ni/M_xO-ZrO_2 active and stable catalysts prepared by Flame Spray Pyrolysis

Matteo Compagnoni,[1] Antonio Tripodi,[1] Alessandro Di Michele,[2] Paola Sassi,[3] Michela Signoretto,[4] Ilenia Rossetti[*1]*

[1] Chemical Plants and Industrial Chemistry Group, Dip. Chimica, Università degli Studi di Milano, INSTM Unit Milano-Università and CNR-ISTM, via C. Golgi, 19, I-20133 Milano, Italy

[2] Dip. Fisica e geologia, Università degli Studi di Perugia, via Pascoli, Perugia, Italy

[3] Dip. Chimica, Biologia e Biotecnologie, Università degli Studi di Perugia, via Elce di Sotto 8, Perugia, Italy

[4] CatMat Lab., Molecular Sciences and Nanosystems Dept., Ca' Foscari University, INSTM Unit, Campus Scientifico, via Torino,155 30172 Mestre (VE) (Italy).

ABSTRACT

Steam reforming of hydrocarbons is a mature technology and its implementation on other substrates such as bio-ethanol appears as a ready opportunity to produce H_2 from renewable sources. The Low Temperature Ethanol Steam Reforming (LT-ESR, 300-500°C) could be a really efficient technology from the energetic point of view. However, deactivation by coke deposition remains the biggest issue, due to inefficient carbon gasification by steam in such low temperature range. We demonstrated the feasibility of the process at low temperature taking into account both activity and deactivation issues. The attention was focused on the addition of basic promoters and on the development of an

[*] Corresponding authors: I. Rossetti, ilenia.rossetti@unimi.it, Fax: +39-02-50314300

unconventional preparation procedure, in comparison with a traditional precipitation/impregnation route, to improve stability and activity.

Therefore, in this work several catalysts were studied, differently promoted by alkali and alkali earth oxides (CaO, MgO, K_2O) using a non conventional doping method. H_2 yield and selectivity to CO demonstrated tightly related to the promoter adopted. Flame Spray Pyrolysis synthesis of nickel nanoparticles stabilized in a zirconia matrix ($Ni/M_xO–ZrO_2$) was performed, obtaining more stable catalysts toward deactivation by coking with respect to the analogous prepared by traditional precipitation/impregnation. The effect of the doping using a scalable one-pot technique were investigated by means of characterization of fresh catalysts and activity testing. Catalyst resistance toward deactivation was studied by SEM-EDX, TEM, Raman spectroscopy and temperature programmed analysis. Among the promoters, CaO and K_2O showed the best performance, producing a reformate with low CO/CO_2 ratio and, thus, leading to higher H_2 yield with consequent lower impact on H_2 purification in an integrated process. K_2O deeply modified the chemical behaviour of the catalyst allowing to achieve a significant H_2 production also at very low temperature (300°C).

Keywords*: Low Temperature Ethanol Steam Reforming; Coke Formation; Flame Spray Pyrolysis; Alkali Doping; Ni-based catalysts; Catalyst Deactivation; ZrO_2; Process intensification.*

1. Introduction

There is a pressing need to underpin the sustainable and economic growth of a biofuel-based industry that can put together the rising fuel demand with urgent environmental issues [1]. Hydrogen is the ideal energy carrier to solve distributed emissions problems and there is increasing interest for effective alternatives to produce it safely and cleanly from renewable sources [2]. However, efficient processes should be developed for its production and process intensification is a pivotal step for the

economic sustainability of the proposed technologies. Among the various achievable and renewable feedstocks, bioethanol is considered at least since 10-15 years a promising raw material, because it can be produced by biomass fermentation and it is expected to be available industrially on a large scale in the near future from second generation biomass [2,3]. Hence, Ethanol Steam Reforming (ESR) represents a promising way to produce hydrogen thermo-catalytically, though the process needs heat input due to the endothermicity of the reaction. The possibility to work at Low Temperature (LT) is very interesting for this process, due to the much lower thermal energy need, which leads to lower operational costs (thus process intensification), and to avoid catalyst de-activation through sintering, easily occurring at the commonly used high temperatures (T > 650 °C) [4]. Moreover, the CO concentration in the outlet gas is strongly reduced at low temperature due the contribution of the exothermal Water Gas Shift (WGS) reaction. Therefore, the research of catalysts which promote as much as possible the Steam Reforming of Ethanol at Low Temperature (LT-ESR) is very challenging. The application of the process in demonstrative stage is already accomplished [5,6], so that the optimisation of catalyst formulation and process intensification are now required.

The reaction network is usually affected by the formation of several by-products, thus reducing the selectivity to hydrogen and possibly leading to the formation of coke, especially at low temperature where C gasification is not favoured [7]. Besides tuning the operating conditions, the use of highly active and stable catalysts plays a crucial role, overcoming the activity and selectivity aspects, due to the much easier reformation of ethanol with respect to other substrates such as methane or heavier hydrocarbons [4].

Carbon deposition can occur through three different pathways: i) decomposition of hydrocarbons; ii) CO disproportion (Boudouard reaction); iii) olefins polymerization. During the LT-ESR, coking occurs mainly by the last two routes, because the former is a strongly endothermal process, prevailing at higher temperature (650-800°C), only [8]. Ethylene is the main olefin generated during the process, as result of the ethanol dehydration, favoured over acid sites, while CO disproportion strongly

depends on the selectivity of the catalysts and on the presence of CO_2 [9]. In addition, not only the source, but also the nature of the carbon formed is fundamental. Carbon can either be found as ordered (filamentous or graphitic) or amorphous structures [4].

In primis, the support plays a crucial role towards coking resistance, thanks to its own acid-base character and to metal-support interactions [10]. The modification of the support properties can be done choosing carriers with basic/amphoteric features such as La_2O_3, TiO_2, MgO [11–14], or combining different properties by doping [15–17]. ZrO_2 has been proposed as valuable support for the catalytic reforming of methane [18,19] and oxygenated compounds [20,21]. Its beneficial features are attributed to the steam adsorption ability, which promotes water activation and coke gasification. Strong metal-support interaction can be also achieved when nickel is used as active phase [22]. In addition, the high thermal stability of this material allows its use in thermocatalytic processes [12].

A criticism is represented by its intrinsic acidity, usually of Lewis type, possibly leading to ethanol dehydration and polymerisation to form coke. Doping with alkali and alkali-earth metal oxides can be a suitable way to improve the catalyst stability toward deactivation phenomena. Basic doping has been previously investigated in the case of catalysts prepared by traditional wet-methods, such as incipient wetness impregnation, co-precipitation and sol-gel methods [23–29]. This strategy has been selected here to prepare MO_x-modified zirconia (M=Ca, Mg, K) as a support for LT-ESR, in order to couple its water activation properties with a limited acidity, to prevent extensive coking.

Nickel was added as active phase, because of its very high activity and selectivity among non-noble metals, coupled with much lower cost and availability for industrial and commercial purposes [3,16,30]. However, poor resistance to carbon formation with respect to noble metals, forced to find alternative preparation strategies because of the tight correlation between the coking phenomena and support properties or metal dispersion [12,31–33].

The Flame Spray Pyrolysis (FSP) technique is a powerful method for the scalable synthesis of nanostructured materials [34], since it allows the simultaneous synthesis and calcination of oxide

nanomaterials. The transfer from the laboratory level to the plant scale concerning flame aerosol process is nowadays a very intriguing point due to the easy scalability of this one-pot synthesis if the key parameters are properly controlled. Pilot scale reactor and economic analysis carried out by Wegner and co-workers [34,35] for zirconium oxide further enhanced the interest toward this non-conventional synthesis. This may allow overcoming major drawbacks of traditional preparation processes, such as the long processing time, batch-to-batch synthesis and uneasy control over active phase dispersion. By contrast, flame- and aerosol-based processes offer the advantages of simple and often lower cost synthesis, with a continuous production process combined with a short processing time [36].

The main goal of this work was to demonstrate the feasibility of low temperature ethanol steam reforming addressing both the activity and deactivation issues. To do this, we focused on a specifically developed preparation procedure and on catalyst doping with alkali and alkali-earth ions. FSP was therefore employed in this work for the synthesis of the materials as a key to impart strong metal-support interaction and high metal dispersion [37]. These have been proved key points to ensure sufficient resistance to coking for this application. Indeed, the carbides accumulation at the interface between metal particles and support, the main step for the growth of carbon nanofilaments, can be conveniently limited if small Ni particles are obtained and kept stable by strong metal support interaction (SMSI). Thus, the detailed characterisation of the prepared catalysts, mainly by electron microscopy and TPR, allow to correlate resistance to coking with metal support interaction and metal dispersion, as a way to improve catalyst durability.

The basic doping of the support by means of FSP was also addressed here and related to the catalytic results. CaO, MgO and K_2O were chosen as basic promoters for ZrO_2 in order to limit the role of surface acidity on coking. Also in this case, tuning the acid-base character of the catalyst, but also contributing to peculiar redox properties, the attention was addressed to improve operational stability. The loading of promoter and active metal (Ni) were chosen considering our best previous results,

obtained by using conventional preparation procedures [38]. The samples were tested for the LT-ESR (300-500°C), representing a mean for process intensification, but being very critical for carbon formation, especially when using, as in this case, stoichiometric steam-to-carbon ratio (S/C) as overstressing condition. Comparison with the catalysts prepared by an alternative precipitation-impregnation method was also carried out. The characterisation of the spent materials allowed to identify the most durable candidate catalyst and optimal reaction conditions.

2. Experimental

2.1. Preparation of Ni/M_xO-ZrO_2

Ni-based catalysts were prepared by FSP using a home-made apparatus, comprehensively described elsewhere [39,40]. Samples were prepared diluting Zirconium acetyl-acetonate (Aldrich, pur. 98%), the alkaline precursor and Nickel (II) acetate tetrahydrate (Aldrich, pur. 98%), in a mixture 1:1 (vol/vol) of o-xylene (Aldrich, pur. >98%) and propionic acid (Aldrich, pur. 97%), with a 0.22 M final concentration. Alkaline precursors were: Calcium acetate (Aldrich, pur. >99%), Magnesium acetate (Aldrich, pur. >99%) and Potassium acetate (Baker, pur. >99%). The proper concentration of the precursors solution was chosen in order to optimize the opposite effect of production rate (favoured by higher concentration of the precursors) and aggregation phenomena (more likely with increasing particle density in the flame) [39]. Preparations were carried out to achieve 10 wt.% Ni loading and 4 wt.% M_xO in the zirconia matrix. The solution was fed to the burner using a 50 ml glass syringe with a flow rate of 2.2 ml/min and a 0.7 bar pressure drop across the nozzle, cofed with 5 l/min of O_2. Ni/M_xO-ZrO_2 catalysts with the following composition were prepared: Ni 10 wt.% / ZrO_2 (labelled as Zr-Ni); Ni 10 wt.%/ CaO 4 wt.% - ZrO_2 (labelled as CaZr-Ni); Ni 10 wt.% / MgO 4 wt.% - ZrO_2 (labelled as MgZr-Ni); Ni 10 wt.% / K_2O 4 wt.% - ZrO_2 (labelled as KZr-Ni). The concentration was selected based on a preliminary screening and based on precursors solubility in the mother solution. The expected value of flame temperature, *ca*. 1500°C [41,42], was ensured by the

selected propionic acid / o-xylene ratio and the decomposition of acetate precursors, whose combustion contributes to increase the total combustion enthalpy, and by selecting proper pressure drop across the nozzle (ΔP = 0.7 bar), liquid and oxygen flowrates. The use of acetates as metal precursors was chosen considering their better solubility with respect to nitrate in the selected solvent mixture [39,42], and their further contribution to the combustion enthalpy.

Additionally, a precipitation-impregnation technique was used (PC). $Zr(OH)_4$ was prepared by a precipitation method [43] at a constant pH of 10. $ZrOCl_2*8H_2O$ (Sigma–Aldrich, purity ≥99.5%) was dissolved in distilled water and added with a peristaltic pump under vigorous stirring to an ammonia (33%, Riedel-de Haën) solution. During the precipitation, the pH value was kept constant at 10.0 ± 0.1 by the continuous addition of a 33% ammonia solution. After the complete addition of the salt solution, the hydroxide suspension was aged for 20 h at 90 °C, then filtered and washed with warm distilled water until it was free from chloride ions ($AgNO_3$ test). The samples were dried overnight at 110 °C. $Zr(OH)_4$ was impregnated with an aqueous solution containing both the metal ($Ni(NO_3)_2*6H_2O$, Sigma–Aldrich, purity ≥98.5%) and the dopants ($Ca(NO_3)_2*4H_2O$, Fluka, purity ≥99%, KNO_3, Fluka, purity ≥99%,) precursors. The active phase (Ni) and the dopants (CaO and K_2O) were added to $Zr(OH)_4$ simultaneously by means of the incipient wetness impregnation technique. Ni was added at the loading of 10 wt%, whereas CaO and K varied at 9 wt%. This amount of promoter has been optimised in a previous work [38]. The samples were dried overnight at 110 °C and finally heated (2 °C/min) up to 500 °C in flowing air (30 mL/min STP) and kept at this temperature for 4 h.

2.2. Catalysts characterization

X-ray powder diffraction (XRD) analysis was carried out at room temperature by means of a PHILIPS PW3020 diffractometer with Bragg-Brentano θ - 2θ geometry with the CuKα radiation (λ = 1.5406 Å). Intensities were collected over a 21° – 90° 2θ range with 0.03° step size and 4 s step time. The

apparatus was provided with graphite monochromator. The voltage and current intensity of the generator were set at 40 kV and 30 mA respectively. The surface area and porosity distribution were determined by N_2 adsorption-desorption at -196 °C using a Micromeritics ASAP 2020 instrument. Surface area was calculated on the basis of the Brunauer, Emmet and Teller equation (BET), while the pores size distribution was determined by the BJH method, applied to the N_2 desorption branch of the isotherm. Prior to the analysis the samples were outgassed at 300°C for 24 hours.

TPR (Temperature Programmed Reduction) measurements were performed by placing the catalyst in a quartz reactor and heating by 10°C min^{-1} from r.t. to 800°C in a 10 vol% H_2/N_2 gas stream flowing at 40 ml/min.

Temperature Programmed Oxidation (TPO) experiments were run placing the spent catalysts in a quartz reactor. The temperature was ramped at a rate of 10 °C min^{-1} from r.t. to 800 °C in 10 vol% O_2/He gas stream flowing at 40 mL min^{-1}.

Deconvolution of the peaks was carried out by means of the Origin Pro 9.0 software. The number of peaks was chosen considering the best fitting of the whole curve using Gaussian functions.

SEM images have been obtained using a Field Emission Gun Electron Scanning Microscopy LEO 1525, after metallization with Cr. Elemental composition was determined using a BrukerQuantax EDS.

TEM images of spent samples have been obtained using a Philips 208 Transmission Electron Microscope. The samples were prepared by putting one drop of an ethanol dispersion of the catalysts on a copper grid pre-coated with a Formvar film and dried in air.

Micro-Raman sampling was made by an OLYMPUS microscope (model BX40) connected to an ISA Jobin–Yvon model TRIAX320 single monochromator, with a resolution of 1 cm^{-1}. The source of excitation was a Melles Griot 25LHP925 He Ne laser that was used in single line excitation mode at λ = 632.8 nm. The power focused on the samples was always less than 2 mW. The scattered Raman

photons were detected by a liquid-nitrogen cooled charge coupled device (CCD, Jobin Yvon mod. Spectrum One).

2.3. LT-ESR activity testing

Activity tests were performed by means of a micropilot plant constituted by an Incoloy 800 continuous downflow reactor (i.d. 0.9 cm, length 40 cm), heated by an electric oven. Temperature was controlled by an Eurotherm 3204 TIC. The reactor was fed with gaseous reactants. The catalysts were pressed, ground and sieved into 0.15–0.25 mm particles and *ca.* 0.5 g were loaded into the reactor after dilution 1:3 (vol/vol) with SiC of the same particle size. Catalyst activation was accomplished by feeding 50 cm^3 min^{-1} of a 20 vol% H_2/N_2 gas mixture at 500 °C for 1 h. During activity testing 0.017 cm^3 min of a 3:1 (mol/mol) water/ethanol liquid mixture were fed to the reactor by means of a Hitachi, mod. L7100, HPLC pump, added with 57 cm^3 min^{-1} of N_2, used as internal standard, and 174 cm^3 min^{-1} of He. The liquid mixture was vaporised in the hot inlet of the reactor before reaching the catalyst bed. Such dilution of the feed stream was calibrated so to keep the reactants mixture in the vapour phase even at zero conversion at the reactor outlet. The activity tests were carried out at atmospheric pressure, with a Gas Hourly Space Velocity (GHSV) of 2700 h^{-1} (referred to the water/ethanol gaseous mixture) at 300, 400 and 500°C. The testing sequence was carried out starting progressively from the highest temperature in order to avoid possible deactivation by coking of the samples. Analysis of out-flowing gas was performed by a gas chromatograph (Agilent, mod. 7980) equipped with two columns connected in series (MS and Poraplot Q) with a thermal conductivity detector (TCD), properly calibrated for the detection of ethanol, acetaldehyde, acetone, acetic acid, water, ethylene, CO, CO_2, H_2. Repeated analyses of the effluent gas were carried out every hour and the whole duration of every test at each temperature was 8 h. The raw data, expressed as mol/min of each species outflowing from the reactor, have been elaborated as detailed

elsewhere [12,40]. Material balance on C-containing products was used as first hand indicator to evaluate coke deposition.

3. Results and discussion

3.1. Textural, structural and morphological properties

In order to investigate the crystalline phases present in the catalysts, XRD analyses were carried out. XRD patterns of the samples (Fig. 1) showed only the tetragonal phase of zirconia in the case of Zr-Ni, CaZr-Ni and MgZr-Ni, characterized by the most intense peak at $2\theta \approx 30°$, while mixed tetragonal and monoclinic zirconia phases were obtained for KZr-Ni. Although the tetragonal stabilization of zirconia after the addition of CaO and MgO is in accordance with the materials prepared by traditional methods [38,44], the presence of the same structure for the undoped sample suggested that the metastable phase can be effectively synthesized by FSP. On the contrary K-promotion led to a mixed phase. The stabilization effect of potassium for zirconia support is not clearly reported in literature. For instance, Li and co-workers reported the stabilization of the monoclinic phase for catalysts prepared by impregnation [45]. Generally, the polymorph phase of the flame prepared materials is tightly related with the residence time and temperature achieved during the synthesis [46], but also the dopant nature is fundamental. Mueller et al. [47], in a study on metal-free zirconia nanoparticles prepared by flame pyrolysis at different production rates, showed the correlation between phase composition and synthetic flame parameters. In particular, they found the highest content of tetragonal phase for the smallest particles and for the fastest quenching of the particles during their formation within the flame. The progressive increase of particle size led to an increase of the monoclinic phase, *i.e.* the stable phase at r.t. and atmospheric pressure for coarse grained zirconia [48]. This effect is known as Gibbs–Thomson effect and it can explain phase composition of sample KZr-Ni, indeed characterized by bigger particle size (*vide infra*). Ni crystal size, calculated from the Scherrer equation, is also reported in Table 1. The Ni particle size is particularly important for this

application because it is well known that big ni particles are more prone to form carbon nanotubes than very well dispersed nanoparticles [4] . From this point of view, no significant variation of Ni particle size was achieved when doping with Ca or Mg, whereas a general increase of both ZrO_2 and Ni crystal sizes was observed upon K-doping.

The presence of MgO and CaO crystalline phases revealed their partial segregation. This contrasts with the conclusions reported by Asencios et al. [49] for doped samples prepared by wet methods, where they found only the formation of solid solutions without any dopant's crystalline phase. Phase segregation here observed are ascribed to aggregation mechanisms of the precursors inside the flame. That is why we selected a low promoter loading with respect to materials prepared by precipitation-impregnation.

BET/BJH models were employed to calculate the specific surface area (S_{BET}), porosity and pore size distribution of the catalysts and the results are reported in Table 1. For all the materials a type IV isotherm was observed, with a characteristic hysteresis of materials containing slit-shaped pores or aggregates of platy particles [50]. These results were consistent with the FSP preparation adopted, which lead to the formation of particles in the nanometric size without large intrinsic mesoporosity [51], directly related to the decomposition mechanism of the oxide precursors within the flame and the subsequent agglomeration [39]. The porosity of the samples was not significant, because the single nanoparticles are essentially dense and some mesoporosity only results from particle agglomeration in the flame during the synthesis.

No significant difference between the adsorption/desorption isotherms shape of doped and undoped samples was evidenced. However, almost halved S_{BET} was obtained for KZr-Ni with respect to other samples. This result could be explained by different rearrangements during the particles agglomeration within the flame and by surface covering of potassium oxides produced at high temperature, in accordance with Pratsinis and co-workers [52], who revealed this effect for K-Rh/Al_2O_3 catalysts prepared by FSP for the CO_2 hydrogenation process. Ultimately, the effect can be

searched in the different volatility of the alkali and alkali-earth oxides adopted (T_{melt} CaO = 2613°C, T_{melt} MgO = 2825°C, T_{melt} K_2O = 740°C) [53].

H_2-TPR analysis provides a quick characterization to evaluate the effect of a dopant on the reducibility of the active metal oxide [54]. TPR signals are strongly influenced by metal particle size, dispersion and strength of interaction with the support, as extensively described in the literature [38,55]. The H_2 consumption due to the reduction of the support was ruled out in agreement with the analysis of bare ZrO_2 [56] and the H_2 consumption quantification is reported in Table 1. The reduction patterns during temperature increased showing differences in the NiO reduction profiles depending on the promoters added to the zirconia support (Fig. 2). The peaks deconvolution is reported in the Supplementary Information (Fig. S2 and S3).

In the Zr-Ni TPR profile two main peaks were detected, due to NiO strongly and weakly interacting with the zirconia support [57], *i.e*. a sharp peak at 489°C and a shoulder at 385°C, respectively. The weak signal at 258°C was ascribed to a very small amount of NiO very poorly interacting with the support and aggregated in larger particles.

CaZr-Ni was characterized by two different peaks. A broad one was obtained by the overlap of two different peaks localized at 280 and 409°C. The former was attributed to NiO interacting with ZrO_2 influenced by oxygen vacancies due to the presence of CaO in the zirconia framework, as extensively explained elsewhere [38,58]. The latter was attributed to the NiO only interacting with bare ZrO_2. This means that doping with CaO by FSP led to the same effect of partial substitution Zr^{4+}/Ca^{2+} achieved by the traditional impregnation preparation route and, in such case, positively affecting activity and resistance to coking [38].

On the contrary, a broad reduction band in the 370 °C and 700 °C range was detected for MgZr-Ni. The sharper peak at 409 °C was assigned to the reduction of Ni^{2+} species located on the MgO-ZrO_2 surface [50]. The broad band in the range 500°C-750°C was instead related to the reduction of several

complex species in a solid solution of NiO-MgO-ZrO_2 (Ni^{2+}–O–Mg^{2+}) in accordance with a study of Garcia *et al.* [44] and Wang *et al.* [59].

Several peaks were detected also in the case of KZr-Ni. This reduction profile is typical when there is not a narrow particle size distribution and several species are reduced. The possible contribution of K^+ reduction was ruled out considering the quantification of the TPR signals (Table 1). XRD patterns, according to the Gibbs-Thomson effect, and BET analysis, according to the lowest S_{BET}, confirm the highest heterogeneity of particle size for this sample considering ZrO_2 particles, and this fact consequently reflected on active phase dispersion as it could be seen in the TPR curve. However, this aspect did not explain peaks at very high reduction temperature (maximum at 586°C). The latter effect is explained by a strong enhancement of the interaction strength between NiO and ZrO_2 following K doping, in agreement with the stabilization effect of K addition [60] and its direct interaction with the transition metals in the lattice [61].

From a quantitative point of view, Ni was fully reducible for every sample except for the Mg-doped one, whose H_2 consumption was halved with respect to the other catalysts.

Scanning Electron Microscopy (SEM) and Transmission Electron Microscopy (TEM) have been used to investigate samples morphology (Fig. 3 and 4). This allowed deepening the average Ni values of crystal size obtained by XRD, confirming them especially in case of overlapping reflections, as in the case of NiO/Al_2O_3 [4]. The results confirmed a broader particle size dispersion for KZr-Ni. Although for all the other samples the size of NiO particles (darker spots in the TEM Figure) on the oxide matrix was around 10-20 nm in accordance with the XRD average values, no smaller particles were observed for the K-doped catalyst. In general a good metal dispersion was achieved at this quite high metal loading. Few big particles (size $\geq$ 50nm) can be observed in accordance with the weak TPR signals at very low temperatures for every sample. In order to clarify the absence of K oxide species in the XRD pattern, EDX analysis was carried out (Fig. S1). The results confirmed the presence of this promoter, although difficult to identify through X-ray diffraction, and its amount was 3.3 wt%.

Finally, the property modification of zirconia in the presence of basic dopants such as CaO, MgO and K_2O is already known in literature. However the measure of the surface acidity could reveal some drawbacks and misunderstanding for two main reasons: i) the dopant significantly influences the OH mobility and is also correlated with more critical features such as Ni reducibility, particle sizes and support crystalline phase; ii) the general acidity features of the catalysts are often only partially suppressed by the presence of the dopant [38]; iii) Besides interaction with Ni as above discussed, support acidity is correlated to the formation of amorphous coke over support surface, This affects oxygen mobility, but it brings to a modification of catalyst performance that can be reversible or easily tunable by adding steam or oxygen. The most detrimental coking phenomenon is ascribed to the formation of nanotubes, which bring to the physical detachment of the active phase from the support and to the clogging of the reactor.

3.4. Catalytic activity testing for LT-ESR

To unravel the different possible contributions for the catalyst deactivation, critical steam/ethanol ratio (S/E=3 mol/mol) for coke deposition was chosen, corresponding to the stoichiometric composition. This aspect must be taken into account because also ethanol conversion and H_2 production are related with this important operating parameter [62]. In particular, higher S/E ratio favours the Water Gas Shift equilibria (higher yields of H_2 and CO_2) [8]. Space velocity was chosen in agreement with previous work [38] in order to operate under kinetic control. Hydrogen was used as reducing agent during catalyst activation and temperature was chosen below the Tammann temperature of Nickel (590 °C) in order to limit metal sintering. Blank tests were also conducted using a reactor filled only with quartz and SiC. The results were averaged between 4-8 hours, *i.e.* under steady state conditions, for tests at 400 °C and 500 °C, as reported in Table 2.

The expected equilibrium data were calculated for the chosen operating conditions as reference. They were calculated using the ASPEN Plus® package choosing a Gibbs reactor and selecting as possibly present species all the observed products and byproducts. Identical products distributions were obtained when simulating the reactor as an Equilibrium block, where selected reactions take place. The proposed reactions were:

$CH_3CH_2OH + H_2O \rightarrow 2\ CO + 4\ H_2$ (1) $\Delta H^0_{298} = +\ 255.2$ kJ mol^{-1} [63]

$CO + H_2O \leftrightarrows CO_2 + H_2$ (2) $\Delta H^0_{298} = -\ 41.2$ kJ mol^{-1} [63]

$CH_3CH_2OH \rightarrow CH_4 + CO + H_2$ (3) $\Delta H^0_{298} = +\ 49.0$ kJ mol^{-1} [63]

$CH_3CH_2OH \leftrightarrows CH_3CHO + H_2$ (4) $\Delta H^0_{298} = +284.9$ kJ mol^{-1} [64]

$CH_3CH_2OH \leftrightarrows CH_2CH_2 + H_2O$ (5) $\Delta H^0_{298} = +\ 45.0$ kJ mol^{-1} [65]

$CH_3CHO \rightarrow CH_4 + CO$ (6) $\Delta H^0_{298} = -79.5$ kJ mol^{-1} [64]

Where steps 1, 3 and 6 are considered unlikely to occur in the reverse sense in the operating conditions window adopted. No significant differences were achieved when adding the Boudouard and the methanation reactions.

According to the results reported in Table 2, one may notice that full ethanol conversion is expected at every temperature and that the most favoured pathway based on thermodynamic considerations would be reaction 3, leading to methane, which is the most stable compound at low temperature.

At 500°C every catalyst showed full ethanol conversion and equally negligible selectivity to common by-products such as acetaldehyde and ethylene, as prescribed by thermodynamics. However, lower methane formation was obtained, suggesting that the catalyst would inhibit the bare thermal

decomposition route (reaction 3), favouring other intermediate paths towards H_2, CO and CO_2. Considering a possible mechanism for ethanol conversion over metal particles, one may consider adsorption of ethanol, C-C bond cleavage and progressive loss of hydrogen leaving adsorbed CH_x. The latter should be further oxidised by activated oxygen or oxydril species, possibly before the formation of carbides, which easily migrate through the metal lattice and are responsible of carbon nanotubes formation. According to this mechanism we can propose the hypothesis that our catalysts favour a fast oxidative path, inhibiting the recombination possibility between adsorbed CH_3 and H entities. This can explain the lower methane selectivity with respect to thermodynamics predictions.

The absence of ethylene, which is a coke precursor, could be explained in two ways: i) all the ethylene possibly formed through ethanol dehydration is reformated and/or oligomerized to coke over the catalyst surface; ii) the materials adopted had very low activity for ethanol dehydration. Mattos *et al.* explained this behaviour as direct consequence of the basic nature of the support when using La_2O_3 [8]. However, the whole properties of the catalysts, metal activity combined with support interactions, should be considered [66].

Ethylene was detected in the reactor outlet gases only for the MgZr-Ni sample. At 500°C and 400°C a constant increase of ethylene yield was observed with a decrease of the ethanol conversion for this sample (Fig. 5). This showed a progressive coking over catalyst surface. The formation of carbon suppressed the steam reforming reaction leading to the lowest hydrogen productivity obtained among all the samples. Moreover, the presence of acetaldehyde, product of dehydrogenation, suggested its incomplete reforming at 400°C. However, the high C-balance could mean that also alternative deactivation phenomena were happening. One possibility is the loss of the alkaline promoter during the tests and subsequent enhancement of acidity, progressively increasing ethylene productivity. Alkali loss at temperature higher than 300°C could happen during the steam reforming if the interaction with the support is too weak [67]. This can be a significant problem not only for the stability of the catalyst, but also for the promotion of stress corrosion in stainless steel in the coldest

parts of the plant downstream the reactor. Especially in the case of MgO, steam can react with the oxide and volatilize the alkali through formation of the hydroxide (T_{melt} $Mg(OH)_2$ = 350°C [53]) :

$MgO + H_2O \leftrightarrows Mg(OH)_2$ $\Delta H^0_{298} = -81.3$ kJ mol^{-1}

Energy-Dispersive X-ray spectroscopy (EDX) was used to check the Mg loading after use. Fig. 6 showed that the spent catalyst maintained a good Mg dispersion, without any significant loss of the promoter with respect to the fresh catalyst. This is expected from literature data [67], because the steam partial pressure here used was lower and temperature higher with respect to those needed for the hydroxide formation.

Another possible cause to interpret the poor activity of the Mg-doped catalyst can be an incomplete activation treatment. TPR profile suggests that the activation by reduction at 500°C did not allow to reduce all the nickel oxide and consequently the activity was reduced. To clarify this point activation at 800 °C was also carried out, but no significant increase of hydrogen productivity was detected by repeating the activity test at 500 °C. However, quantitative TPR data showed that even at 800 °C not all the nickel was reduced. The main reason for low and decreasing activity of the Mg-doped sample was here correlated with the increase of ethylene formation and ascribed to the progressive formation of encapsulating carbon, which consequently deactivated the metal particles, as better clarified in the next section.

The incomplete reduction of nickel oxide occurred also in the case of KZr-Ni [68]. However, when comparing this with a K-doped sample prepared by impregnation (*vide infra*) and much more reducible, the activity performance at low temperature was comparable. K doping led to a strong metal-support interaction, as testified by the highest reduction temperature, and this point can be associated to the high activity exhibited by this sample. Frusteri et al. very well explained the beneficial role of K, because of the electronic enrichment of the active phase depressing carbon

formation [13]. We have also drawn similar conclusions for alkali doped catalysts for different applications [69–71].

The CO/CO_2 ratio is considered as a parameter to evaluate the extent of the Water Gas Shift reaction (WGS, reaction 2). WGS reached nearly equilibrium products distribution at 500°C for the Ca-doped sample (CO/CO_2 ratio in Table 2). By contrast, at 400°C the WGS reaction was more favoured from a thermodynamic point of view, but more limited kinetically. CaZr-Ni and KZr-Ni revealed the lowest CO/CO_2 ratio and, accordingly, the highest H_2 productivity at such a temperature. The local defect structures formation in the case of CaZr-Ni increase the oxygen-ion conduction and enhance the formation of active oxygen-containing species through water activation [72]. This may favour the oxidative paths with respect to reaction 3, which would be even more thermodynamically favoured at low temperature (higher methane selectivity calculated at equilibrium).

KZr-Ni showed the best performance in terms of H_2 productivity and low CH_4 selectivity. The beneficial impact of K on Ni-based catalyst toward methane activation and inhibition of methanation was in accordance with Rostrup-Nielsen *et al.* [73]. Experimental results confirmed the DFT-calculations concerning the strong dipole moment induced in the transition state of the dissociating methane molecule with an increase of the energy barrier for dissociation of methane and hence the formation of adsorbed carbon atoms, precursors of coke [73].

The apparently low methane selectivity in the case of MgZr-Ni was only due to the high selectivity towards acetaldehyde, and in turn, the increasing selectivity to C_2 by-products can be correlated to Ni deactivation by coking (encaspsulating carbon).

The formation of coke is the most critical point for LT-ESR as mentioned in the Introduction. Material balance on C-containing products was checked to quickly quantify coke deposition during the tests. The C balance during blank tests was *ca.* 91% at 500°C and 100% at 400°C. The addition of Ca and K promoters decreased the carbon loss, especially during the tests at 400°C (Table 2), while reproducing C balance equal to the blank test at 500°C. The importance of these results increased

comparing them with our previous data on other active phases and supports [12,74]. The beneficial role imparted by these dopants concerning the oxygen mobility, the reduction of surface acidity and the improved H_2O and CO_2 adsorption [8,38] were exploited by using the FSP preparation technique.

It should be remarked that some materials were prepared by us by FP, characterised by higher H_2 productivity (up to ca. 1.8 mol H_2 / min kg_{cat}) [75]. However, the present samples show lower selectivity to byproducts and lower coking rate, besides being more active at lower temperature.

Hydrogen productivity and H_2/CO *vs*. t-o-s are reported in Fig. 7. These parameters are very important because, besides improving H_2 yield, they allow to decrease the impact of the downstream H_2 purification through CO-removal steps, such as the dedicated WSG reactors [76,77]. By contrast, an higher value of CO in the stream means catalysts more suitable for the syngas production dedicated to the Fischer−Tropsch (FT) process, which need a ratio of approximately 2 to obtain high molecular weight paraffin/olefin liquid transportation fuels [78,79]. CaZr-Ni and KZr-Ni revealed the best H_2 yield and lowest CO productivity. However, a progressive decrease of the H_2/CO ratio was observed at 400°C, whereas the respective tests at 500 °C (not reported) revealed a flat pattern with time-on-stream centred around the mean values of Table 2. Two possible causes may coexist: i) the progressive decrease of activity toward H_2 formation by WGS and ESR reactions due to deactivation by coking; ii) the progressive increase of the Reverse Boudouard (RB) reaction due to the carbon possibly accumulated ($CO_2 + C \leftrightarrows 2CO$). The increase of C-balance and H_2 production ruled out the former hypothesis. The 2nd hypothesis seems the most probable because of the positive effect of alkaline additives to prevent the Boudouard reaction and consequently favour the RB pathway, in agreement with Galetti and co-workers and their study on basic ceria doping [80]. Although can be not unexpected this attribution due to the endothermicity of the reaction [81], the presence of this type of reaction on Zr-promoted catalysts was revealed also by Debek et al., studying dry reforming at low temperature [19].

The detected high activity for the WGS reaction was compared also with some representative articles in the open literature. Prasongthum et al. obtained higher values of CO selectivity using Ni/silica fiber catalyst prepared by electrospinning technique [82] with full ethanol conversion, but without specifying the space velocity, so preventing a sefe comparison with the present data.

In order to have a clear overview and an explicit comparison of the catalyst performance considering tests not limited by full conversion, a test with the best catalyst KZr-Ni was performed using a tenth of the catalyst weight used in the activity tests previously shown. The resulting Gas Hourly Space Velocity was 13800 h^{-1}, allowing a direct comparison also with literature data, and the activity results are reported in Fig. 8. The average conversion was 42 ± 4 %. A slightly lower selectivity to hydrogen was obtained, although the general trend and the general good features already discussed above were confirmed. Similar results at lower contact time were obtained by Palma et al. [83], with the same trend in product distributions, though their tests were carried out at higher water/ethanol ratio, which would increase the reactivity. He et al. detected better results using Ni/SBA-15 catalysts at the same water/ethanol ratio, although any tests at lower conversion than 100% was carried out at a space velocity almost ten times lower than 13800 h^{-1}, so comparable with the results reported in the present Tables 2 and 3.

Finally, a more challenging temperature was investigated: 300°C. This reaction temperature is not commonly studied because of the very high catalyst activity necessary to achieve significant H_2 productivity. Usually thermodynamically more favourable side reactions occur, such as the ethanol dehydrogenation without subsequent acetaldehyde reforming, or ethanol decomposition/dehydration [8]. Products distribution is reported in Fig. 9. Generally, the low temperature ethanol steam reforming is considered divided in two steps: i) de-hydrogenation of ethanol to acetaldehyde (reaction 4); ii) decarbonylation of acetaldehyde to form CO and CH_4 (reaction 6) [64].

Zr-Ni confirmed that the first step of ESR was constituted by ethanol dehydrogenation (reaction 4), as acetaldehyde was the only C-product obtained. Mattos et al. evidenced the reaction routes for

acetaldehyde on oxide catalysts by means of a comprehensive IR study [8]. One route is the direct decomposition to CO and CH_4 and the other is the hydrogen abstraction from adsorbed acetaldehyde to form acetyl species and their subsequent decomposition leading to CO(g) and CH_3 adsorbed. Adsorbed methyl species should undergo a further hydrogenation step for the methane evolution or consecutive dehydrogenation to the formation of carbon. The product distribution and carbon balance confirmed the presence of both routes. High resistance toward Boudouard reaction for coke formation was witnessed by the absence of CO_2. This pathway was confirmed by Choong et al., because of the surface oxygen sites modification by using CaO as dopant [84], and confirmed that the surface acidity was not the only property changed by doping with alkaline promoters.

KZr-Ni was the only material still active toward H_2 production at this very low temperature. The products were H_2, CO, CO_2 and CH_4. The presence of CO_2 suggests the acetaldehyde steam reforming reaction, which occurs at lower temperature with respect to ethanol SR using suitable catalysts [8][8]:

$$CH_3CHO + 3\ H_2O \rightarrow 5\ H_2 + 2\ CO_2 \qquad (7)$$

Under these operating conditions, doping with K led to a catalyst able to achieve the lowest methane selectivity at 300°C. Methane selectivity represents one of the key points in order to obtain a good SR catalyst for low operating temperatures. Indeed, methane is more difficult to reformate with respect to the oxygenated molecules and its presence decreases the hydrogen selectivity. On the other hand methane selectivity is less sensitive to other important process parameters such as the H_2O/CH_3CH_2OH ratio [85]. Therefore, except for intrinsic catalyst activity and process temperature, S_{CH4} cannot be effectively tuned by manipulating other degrees of freedom[86,87].

The lower concentration of CO with respect to CH_4 could be explained by the higher activity toward CO_x methanation, favoured at low temperature, or by the enhanced WGS reaction, due to the exothermicity of both routes. The non negligible hydrogen presence in the products suggests the last route as the most likely.

3.5. Characterization of spent samples

Qualitative and quantitative analyses were carried out on the used catalysts in order to better investigate the catalyst deactivation by coke formation or sintering. TPO is a useful technique to quantify coke amount [88]. During this temperature programmed analysis under oxidising atmosphere, the carbon species are oxidized at different temperature in accordance with their nature. Usually amorphous carbon is oxidized at lower temperature (200-300°C) whereas carbon nanotubes and graphitic/ordered carbon at higher temperature (400-600°C) [88]. In general, graphite is the most stable phase at low temperatures, while over 400°C, the MWCNTs are the main constituents of the C deposits, as extensively reported in the literature for Co and Ni-based catalysts [21,76]. Nevertheless, amorphous carbon, the less thermodynamically stable species [89], is the one most frequently found on a practical level, because the pathways leading to its formation are much faster. TPO profiles (Fig. 10) ruled out the presence of amorphous carbon and confirmed the presence of carbon whiskers and ordered carbon. The absence of amorphous carbon was probably one of the main reasons to explain the lower deactivation here observed for K and Ca-doped samples with respect to other catalysts prepared by traditional techniques. Indeed ordered carbon, especially in the form of MWCNT, lead to a less evident deactivation because the tip of the metal particle can still remain accessible to the reactants due to the intrinsic mechanism of carbon formation [90]. By contrast, amorphous carbon is always encapsulating and in the presence of metal particles nearby the set up point, it can completely deactivate the active phase.

The discrimination between graphitic carbon in form of nanotubes or graphitic layers in the region between 400-600°C is very complex. TEM and SEM pictures revealed both graphitic and filamentous carbon for all the catalysts (Fig. 11 and 12).

Deconvolution of the TPO profiles was also carried out to attempt an attribution to the different carbon species (Fig.13). All features were formed by the overlap of two peaks, but the position in

terms of temperature changed slightly when varying the catalyst composition. As above mentioned, the higher is the order of the carbon species, the harsher is their oxidation [91]. However, the higher is the amount of carbon, the easier is the ability of the carbon to grow up in increasingly ordered structure. Raman spectroscopy (Fig. 14) pointed out that no significant variation of the D/G bands ratio was detected. Such parameter is usually applied to discriminate between different ordered carbon species. The D/G band intensity ratio here obtained between 1.1-1.3 confirmed the absence of amorphous carbon, because its presence usually leads to D/G intensity ratio higher than 1.8 [91].

The observed shift of the peaks in TPO analysis was therefore attributed to the different carbon amount rather than to significantly different species. The two peaks were attributed to the formation of non-filamentous coke at lower temperature, in particular in the C_β form, and filamentous coke at higher temperature [92]. The C_β form is produced by the rearrangement and polymerization of the C_α form, instead of crystalline phase formation by the dissolution of C_α in Ni particles and diffusion to the interface with the support with subsequent formation of carbon nanotubes. The C_β carbon polymer favours the encapsulation phenomena and leads to a complete de-activation of the Ni particles. For this reason Zr-Ni was less active at 400 and 300°C with respect CaZr-Ni and KZr-Ni, indeed it revealed the most intense 1st peak in TPO analysis.

This explains also the higher activity of KZr-Ni with respect to CaZr-Ni, the former being characterised by an overall lower C deposition with respect to the Ca-doped sample. For MgZr-Ni the low amount of carbon formed was simply due to the lower activity of this catalyst, accumulated over the active phase, and not with the mechanism of carbon formation. Basically, the catalyst is less active towards every reaction, including those bringing to coke precursors. The progressive deactivation revealed during the activity tests were attributed to the encapsulating carbon. This attribution was confirmed by the higher peak intensity of the 1st peak with respect the 2nd one in the TPO deconvolution and by TEM analysis.

To quantify the overall amount of C accumulated during the whole testing, TPO analysis was elaborated after calibration and the results are reported in Fig. 15. In accordance with the C-balance of the activity tests, the lowest amount of carbon was detected for KZr-Ni and MgZr-Ni. As suggested in the Introduction, the strong metal-support interactions detected by TPR analysis confirmed to lead to the lowest carbon formation.

3.6. Comparison of FSP with traditional preparation routes

During this work, in comparison to the traditional doping methods such as incipient wetness impregnation, co-precipitation and sol-gel synthesis [93], we proposed an alternative FSP preparation procedure for the synthesis of doped catalysts. The study of this technique is very interesting because the particles are formed very rapidly and the aggregation mechanism could lead to a different way of doping because the dopant is added in the meantime of the other precursors. This allows possible incorporation of the dopant into the support structure, with formation of oxygen vacancies as reported elsewhere [38]. In order to shed light about this point, the best catalysts in term of H_2 productivity and selectivity, which were as aforementioned the doped by Ca and K, were compared with the homologous catalysts prepared by an optimized precipitation/impregnation method. (Table 3). Detailed characterization of the Ca-doped sample is reported elsewhere [38], whereas TPR, Ni content and specific surface area of the K-doped catalyst are reported in the Supplementary Information file. Considering the Ca doping, a higher hydrogen productivity was achieved at both 500 and 400°C. These results confirmed the theoretical line detailed in the previous sections of this paper about the best activity for this process using Flame Spray Pyrolysis preparation as synthetic route. However a different behaviour concerning methane selectivity was detected, probably due to the limited ethanol decomposition for the impregnated materials. The same feature was obtained for the K doping and better results with respect to Ca were observed, irrespectively of the preparation method. By using the traditional synthetic route the calcination step allowed to tune the metal-support interaction and the dispersion of the active phase. Moreover, calcination temperature and time often led to different

catalytic activity and crystal phase even though the dopant, the host oxide and the precursors were the same [93,94]. During FSP a high calcination temperature is attained depending on the solvent, precursors nature, flow rates and pressure drop within the burner [42]. The mixture of propionic acid and o-xylene adopted allows to achieve a temperature higher than 1000°C [42], and the calcination occurred in few milliseconds after the nucleation step. Ideally by FSP, homogeneous nanoparticles are formed by evaporation of the precursor, its conversion and subsequent nucleation to form the final catalyst. The optimized apparatus allowed to have a proper active phase dispersion for the LT-ESR process, as highlighted by the activity results and the characterization. Anyway, this degree of heterogeneity may be not acceptable for other processes with a very high activity-particle shape correlation, such as the CO oxidation[95]. The major drawbacks of the traditional preparation and doping methods, such as the long processing time and the batch-to-batch synthesis were successfully outdated considering CaZr-Ni and KZr-Ni. Ni nanometric particle size supported on oxide carrier and good average surface area combined with strong metal support interactions were obtained by FSP, in agreement with previous results obtained with different set-up by Mädler *et al.* [96]. The doping agents did not significantly influence Ni particle size or surface area unless in the case of K promoter. Therefore the results proved that the variation of catalytic performance was ascribed mainly to the properties modification imparted by the promoter oxides added.

4. Conclusion

In this work, the possibility to carry out ethanol steam reforming at low temperature was explored, as a step towards the economic feasibility and process intensification. 500 °C is considered a sufficiently low temperature for this process, while 400 °C and 300 °C are often too critical as for insufficient activity and catalyst deactivation. This latter is a key point from an industrial point of view.

As a second goal, the effect of alkali addition on the performance of Ni/ZrO_2 catalyst for the LT-ESR has been investigated. Activity results showed that full ethanol conversion can be achieved even at

400°C with the present catalysts, which thus proved very active for this application. The main differences were observed as for products distribution and resistance to coking. A strong decrease of CO/CO_2 ratio can be achieved by doping the Ni/ZrO_2 with Ca and K oxides. This parameter is fundamental to limit the further purification of reformate gas if the aim is the production of pure hydrogen or reformate with very low CO concentration.

The results witnessed that K_2O was mainly a chemical or electronic promoter rather than a textural promoter. The wider particle size distribution revealed a different agglomeration pathway within the flame during the synthesis. By contrast, the enhancement of activity at 500 °C and 400 °C, and the non negligible activity even at 300 °C, suggested K as one of the best chemical promoters for this process. Furthermore, alkaline promoters did not only affect surface acidity, but also Ni redox properties, crystalline phase and metal-support interactions.

Finally, doped catalysts were prepared by Flame Spray Pyrolysis, a scalable and one-pot synthetic method rather new for this application, which can lead to peculiar catalyst properties. The characterization of fresh and spent samples allowed to correlate the structural modifications of the FSP catalysts by the addition of the promoters with their performance for this process, which has not been previously reported in the literature by this synthetic route.

This work not only provides insights into the ESR process at very lower temperature than conventional (down to 300 °C), but it also provides guidance to develop new doped metal supported catalysts by a one step gas phase combustion synthesis already used routinely in a large scale to make millions of tons of powder single oxides.

ACKNOWLEDGEMENTS

The valuable collaboration of Mrs. Anna Dell'Angelo for the collection of some activity data is gratefully acknowledged.

REFERENCES

[1] Koçar G, Civaş N. An overview of biofuels from energy crops: Current status and future prospects. Renew Sustain Energy Rev 2013;28:900–16. doi:10.1016/j.rser.2013.08.022.

[2] Bilal M, Jackson D. The effect of impurities on the steam reforming of ethanol over ruthenium/alumina. Int J Hydrogen Energy 2014;4:4055–64. doi:10.1016/j.ijhydene.2014.07.139.

[3] He S, Mei Z, Liu N, Zhang L, Lu J, Li X, et al. Ni/SBA-15 catalysts for hydrogen production by ethanol steam reforming: Effect of nickel precursor. Int J Hydrogen Energy 2017;42:14429–38. doi:10.1016/j.ijhydene.2017.02.115.

[4] Christensen KO, Chen D, Lødeng R, Holmen A. Effect of supports and Ni crystal size on carbon formation and sintering during steam methane reforming. Appl Catal A Gen 2006;314:9–22. doi:10.1016/j.apcata.2006.07.028.

[5] Tripodi A, Compagnoni M, Ramis G, Rossetti I. Process simulation of hydrogen production by steam reforming of diluted bioethanol solutions: Effect of operating parameters on electrical and thermal cogeneration by using fuel cells. Int J Hydrogen Energy 2017;42:in press. doi:10.1016/j.ijhydene.2017.04.056.

[6] Casanovas A, Divins NJ, Rejas A, Bosch R, Llorca J. Finding a suitable catalyst for on-board ethanol reforming using exhaust heat from an internal combustion engine. Int J Hydrogen Energy 2017;42:13681–90. doi:10.1016/j.ijhydene.2016.11.197.

[7] Busca G, Montanari T, Resini C, Ramis G, Costantino U. Hydrogen from alcohols: IR and flow reactor studies. Catal Today 2009;143:2–8. doi:10.1016/j.cattod.2008.09.010.

[8] Mattos L V., Jacobs G, Davis BH, Noronha FB. Production of hydrogen from ethanol: Review of reaction mechanism and catalyst deactivation. Chem Rev 2012;112:4094–123. doi:10.1021/cr2000114.

[9] Wang F, Li Y, Cai W, Zhan E, Mu X, Shen W. Ethanol steam reforming over Ni and Ni-Cu catalysts. Catal Today 2009;146:31–6. doi:10.1016/j.cattod.2009.01.027.

[10] Zanchet D, Santos JBO, Damyanova S, Gallo JMR, Bueno JMC. Toward understanding metal-catalyzed ethanol reforming. ACS Catal 2015;5:3841–63. doi:10.1021/cs5020755.

[11] Li H, Zhang L, Dai H, He H. Facile Synthesis and Unique Physicochemical Properties of Three-Dimensionally Ordered Macroporous Magnesium Oxide , Gamma-Alumina , and Ceria - Zirconia Solid Solutions with Crystalline Mesoporous Walls 4421. Inorg Chem 2009;48:4421–34.

[12] Ramis G, Rossetti I, Finocchio E, Compagnoni M, Signoretto M, Michele A Di. Metal Dispersion and Interaction with the Supports in the Coke Production over Ethanol Steam Reforming Catalysts. Prog. clean energy, vol. 1, 2015, p. 695–711. doi:10.1007/978-3-319-16709-1_51.

[13] Frusteri F, Freni S. Bio-ethanol, a suitable fuel to produce hydrogen for a molten carbonate fuel cell. J Power Sources 2007;173:200–9. doi:10.1016/j.jpowsour.2007.04.065.

[14] Mei D, Lebarbier Dagle V, Xing R, Albrecht KO, Dagle RA. Steam Reforming of Ethylene Glycol over MgAl 2 O 4 Supported Rh, Ni, and Co Catalysts. ACS Catal 2015;6:315–25. doi:10.1021/acscatal.5b01666.

[15] Tan M, Wang X, Hu Y, Shang X, Zhang L, Zou X, et al. Influence of nickel content on structural and surface properties, reducibility and catalytic behavior of mesoporous γ-alumina-supported Ni–Mg oxides for pre-reforming of liquefied petroleum gas. Catal Sci

Technol 2016;6:3049–63. doi:10.1039/C5CY01582K.

[16] Liu J, Yu J, Su F, Xu G. Intercorrelation of structure and performance of Ni–Mg/Al 2 O 3 catalysts prepared with different methods for syngas methanation. Catal Sci Technol 2014;4:472–81. doi:10.1039/C3CY00601H.

[17] Ni M, Leung DYC, Leung MKH. A review on reforming bio-ethanol for hydrogen production. Int J Hydrogen Energy 2007;32:3238–47. doi:10.1016/j.ijhydene.2007.04.038.

[18] Chen XJ, Jiang JG, Tian SC, Li KM. Biogas dry reforming for syngas production: catalytic performance of nickel supported on waste-derived SiO2. Catal Sci Technol 2015;5:860–8. doi:10.1039/c4cy01126k.

[19] Dębek R, Galvez ME, Launay F, Motak M, Grzybek T, Da Costa P. Low temperature dry methane reforming over Ce, Zr and CeZr promoted Ni–Mg–Al hydrotalcite-derived catalysts. Int J Hydrogen Energy 2016;41:11616–23. doi:10.1016/j.ijhydene.2016.02.074.

[20] Dömök M, Oszkó A, Baán K, Sarusi I, Erdőhelyi A. Reforming of ethanol on Pt/Al2O3-ZrO2 catalyst. Appl Catal A Gen 2010;383:33–42. doi:10.1016/j.apcata.2010.05.016.

[21] Rossetti I, Gallo A, Dal Santo V, Bianchi CL, Nichele V, Signoretto M, et al. Nickel Catalysts Supported Over TiO 2 , SiO 2 and ZrO 2 for the Steam Reforming of Glycerol. ChemCatChem 2013;5:294–306. doi:10.1002/cctc.201200481.

[22] Wolfbeisser A, Klötzer B, Mayr L, Rameshan R, Zemlyanov D, Bernardi J, et al. Surface modification processes during methane decomposition on Cu-promoted Ni–ZrO2 catalysts. Catal Sci Technol 2015;5:967–78. doi:10.1039/C4CY00988F.

[23] Kusche M, Enzenberger F, Bajus S, Niedermeyer H, Bösmann A, Kaftan A, et al. Enhanced activity and selectivity in catalytic methanol steam reforming by basic alkali metal salt coatings. Angew Chemie - Int Ed 2013;52:5028–32. doi:10.1002/anie.201209758.

[24] Sanchez-Sanchez M., Navarro RM, Fierro JL. Ethanol steam reforming over Ni/MxOyNi/MxOy–Al2O3Al2O3 (M=CeM=Ce, La, Zr and Mg) catalysts: Influence of support on the hydrogen production. Int J Hydrogen Energy 2007;32:1462–71. doi:10.1016/j.ijhydene.2006.10.025.

[25] Chen I, Chen F. Effect of Alkali and Alkaline-Earth Metals on the Resistivity to Coke Formation and Sintering of Nickel-Alumina Catalysts. Ind Eng Chem Res 1990;29:534–9. doi:10.1021/ie00100a006.

[26] Ryczkowski R, Niewiadomski M, Michalkiewicz B, Skiba E, Ruppert AM, Grams J. Effect of alkali and alkaline earth metals addition on Ni/ZrO2 catalyst activity in cellulose conversion. J Therm Anal Calorim 2016;126:103–10. doi:10.1007/s10973-016-5465-z.

[27] Carrero A, Calles JA, Vizcaíno AJ. Effect of Mg and Ca addition on coke deposition over Cu-Ni/SiO2 catalysts for ethanol steam reforming. Chem Eng J 2010;163:395–402. doi:10.1016/j.cej.2010.07.029.

[28] Palma V, Ruocco C, Meloni E, Ricca A. Influence of Catalytic Formulation and Operative Conditions on Coke Deposition over CeO2-SiO2 Based Catalysts for Ethanol Reforming. Energies 2017;10:1030. doi:10.3390/EN10071030.

[29] Shao J, Zeng G, Li Y. Effect of Zn substitution to a LaNiO 3−δ perovskite structured catalyst in ethanol steam reforming. Int J Hydrogen Energy 2017;42:17362–75. doi:10.1016/j.ijhydene.2017.04.066.

[30] Danilova MM, Fedorova ZA, Kuzmin VA, Zaikovskii VI, Porsin AV, Krieger T. Combined Steam and Carbon Dioxide Reforming of Methane over Porous Nickel Based Catalysts. Catal Sci Technol 2015;5:2761–8. doi:10.1039/C4CY01614A.

[31] Harshini, Lee DH, Jeong J, Kim Y, Nam SW, Ham HC, et al. Enhanced oxygen storage capacity of Ce0.65Hf0.25M0.1O2-delta (M=rare earth elements): Applications to methane steam reforming with high coking resistance. Appl Catal B Environ 2014;148–149:415–23. doi:10.1016/j.apcatb.2013.11.022.

[32] Pino L, Vita A, Cipitì F, Laganà M, Recupero V. Hydrogen production by methane tri-reforming process over Ni–ceria catalysts: Effect of La-doping. Appl Catal B Environ 2011;104:64–73. doi:10.1016/j.apcatb.2011.02.027.

[33] Sánchez-Sánchez MC, Navarro RM, Fierro JLG. Ethanol steam reforming over Ni / Mx Oy-Al2 O3 (M = Ce, La, Zr and Mg) catalysts: Influence of support on the hydrogen production. Int J Hydrogen Energy 2007;32:1462–71. doi:10.1016/j.ijhydene.2006.10.025.

[34] Gröhn AJ, Pratsinis SE, Wegner K. Scale-up for Nanoparticle Synthesis by Flame Spray Pyrolysis : The High Temperature Particle Residence Time. Ind Eng Chem Res 2014;53:10734–42. doi:10.1021/ie501709s.

[35] Gröhn AJ, Eggersdorfer ML, Pratsinis SE, Wegner K. On-line monitoring of primary and agglomerate particle dynamics. J Aerosol Sci 2014;73:1–13. doi:DOI 10.1016/j.jaerosci.2014.03.001.

[36] Mädler L, Kammler HK, Mueller R, Pratsinis SE. Controlled synthesis of nanostructured particles by flame spray pyrolysis. J Aerosol Sci 2002;33:369–89. doi:10.1016/S0021-8502(01)00159-8.

[37] Pongthawornsakun B, Mekasuwandumrong O, Prakash S, Ehret E, Santos Aires FJC, Panpranot J. Effect of reduction temperature on the characteristics and catalytic properties of TiO2 supported AuPd alloy particles prepared by one-step flame spray pyrolysis in the selective hydrogenation of 1-heptyne. Appl Catal A Gen 2015;506:278–87. doi:10.1016/j.apcata.2015.09.012.

[38] Nichele V, Signoretto M, Pinna F, Menegazzo F, Rossetti I, Cruciani G, et al. Ni/ZrO2 catalysts in ethanol steam reforming: Inhibition of coke formation by CaO-doping. Appl Catal B Environ 2014;150–151:12–20. doi:10.1016/j.apcatb.2013.11.037.

[39] Chiarello GL, Rossetti I, Forni L. Flame-spray pyrolysis preparation of perovskites for methane catalytic combustion. J Catal 2005;236:251–61.

[40] Rossetti I, Biffi C, Bianchi CL, Nichele V, Signoretto M, Menegazzo F, et al. Ni/SiO2 and Ni/ZrO2 catalysts for the steam reforming of ethanol. Appl Catal B Environ 2012;117–118:384–96. doi:10.1016/j.apcatb.2012.02.006.

[41] Chiarello GL, Rossetti I, Lopinto P, Migliavacca G, Forni L. Preparation by flame spray pyrolysis of ABO3 catalysts for the flameless combustion of methane. Catal Today 2006;117:549–53. doi:10.1016/j.cattod.2006.06.018.

[42] Chiarello GL, Rossetti I, Forni L, Lopinto P, Migliavacca G. Solvent nature effect in preparation of perovskites by flame pyrolysis. 2. Alcohols and alcohols + propionic acid mixtures. Appl Catal B Environ 2007;72:227–32. doi:10.1016/j.apcatb.2006.10.026.

[43] Zane F, Melada S, Signoretto M, Pinna F. Active and recyclable sulphated zirconia catalysts for the acylation of aromatic compounds. Appl Catal A Gen 2006;299:137–44. doi:10.1016/j.apcata.2005.10.019.

[44] García V, Fernández JJ, Ruíz W, Mondragón F, Moreno A. Effect of MgO addition on the basicity of Ni/ZrO2 and on its catalytic activity in carbon dioxide reforming of methane. Catal Commun 2009;11:240–6. doi:10.1016/j.catcom.2009.10.003.

[45] Li ZJ, Prescott H a, Deutsch J, Trunschke a, Lieske H, Kemnitz E. Characterization and catalytic behavior of potassium-modified ZrO2 base catalysts. Catal Letters 2004;92:175–80.

doi:10.1023/B:CATL.0000014342.63805.74.

[46] Strobel R, Pratsinis SE. Flame aerosol synthesis of smart nanostructured materials. J Mater Chem 2007;17:4743–56. doi:10.1039/b711652g.

[47] Mueller R, Mädler L, Pratsinis SE. Nanoparticle synthesis at high production rates by flame spray pyrolysis. Chem Eng Sci 2003;58:1969–76. doi:10.1016/S0009-2509(03)00022-8.

[48] Chraska T, King AH, Berndt CC. On the size-dependent phase transformation in nanoparticulate zirconia. Mater Sci Eng A 2000;286:169–78. doi:10.1016/S0921-5093(00)00625-0.

[49] Asencios YJO, Bellido JDA, Assaf EM. Synthesis of NiO-MgO-ZrO2 catalysts and their performance in reforming of model biogas. Appl Catal A Gen 2011;397:138–44. doi:10.1016/j.apcata.2011.02.023.

[50] Fan M-S, Abdullah AZ, Bhatia S. Utilization of greenhouse gases through carbon dioxide reforming of methane over Ni–Co/MgO–ZrO2: Preparation, characterization and activity studies. Appl Catal B Environ 2010;100:365–77. doi:10.1016/j.apcatb.2010.08.013.

[51] Teoh WY, Doronkin DE, Beh GK, Dreyer JAH, Grunwaldt J-D. Methanation of carbon monoxide over promoted flame-synthesized cobalt clusters stabilized in zirconia matrix. J Catal 2015;326:182–93. doi:10.1016/j.jcat.2015.03.014.

[52] Büchel R, Baiker A, Pratsinis SE. Effect of Ba and K addition and controlled spatial deposition of Rh in Rh/Al2O3 catalysts for CO2 hydrogenation. Appl Catal A Gen 2014;477:93–101. doi:10.1016/j.apcata.2014.03.010.

[53] Haynes WM. CRC Handbook of Chemistry and Physics, 95th ed. 2015.

[54] Bezverkhyy I, Danot M, Afanasiev P. New low-temperature preparations of some simple and mixed Co and Ni dispersed sulfides and their chemical behavior in reducing atmosphere. Inorg Chem 2003;42:1764–8. doi:10.1021/ic026024j.

[55] Song YQ, He DH, Xu BQ. Effects of preparation methods of ZrO2 support on catalytic performances of Ni/ZrO2 catalysts in methane partial oxidation to syngas. Appl Catal A Gen 2008;337:19–28. doi:10.1016/j.apcata.2007.11.032.

[56] Dong WS, Roh HS, Jun KW, Park SE, Oh YS. Methane reforming over Ni/Ce-ZrO2 catalysts: Effect of nickel content. Appl Catal A Gen 2002;226:63–72. doi:10.1016/S0926-860X(01)00883-3.

[57] Angeli SD, Turchetti L, Monteleone G, Lemonidou AA. Catalyst development for steam reforming of methane and model biogas at low temperature. Appl Catal B Environ 2016;181:34–46. doi:10.1016/j.apcatb.2015.07.039.

[58] Bellido JD a, Assaf EM. Nickel catalysts supported on ZrO2, Y2O3-stabilized ZrO2 and CaO-stabilized ZrO2 for the steam reforming of ethanol: Effect of the support and nickel load. J Power Sources 2008;177:24–32. doi:10.1016/j.jpowsour.2007.11.006.

[59] Wang YH, Liu HM, Xu BQ. Durable Ni/MgO catalysts for CO2 reforming of methane: Activity and metal-support interaction. J Mol Catal A Chem 2009;299:44–52. doi:10.1016/j.molcata.2008.09.025.

[60] Frusteri F, Freni S, Chiodo V, Spadaro L, Di Blasi O, Bonura G, et al. Steam reforming of bio-ethanol on alkali-doped Ni/MgO catalysts: hydrogen production for MC fuel cell. Appl Catal A Gen 2004;270:1–7. doi:10.1016/j.apcata.2004.03.052.

[61] Laversin H, Courcot D, Zhilinskaya E a., Cousin R, Aboukaïs A. Study of active species of Cu-K/ZrO_2 catalysts involved in the oxidation of soot. J Catal 2006;241:456–64. doi:10.1016/j.jcat.2006.05.006.

[62] Hou T, Zhang S, Chen Y, Wang D, Cai W. Hydrogen production from ethanol reforming: Catalysts and reaction mechanism. Renew Sustain Energy Rev 2015;44:132–48. doi:10.1016/j.rser.2014.12.023.

[63] Oakley JH, Hoadley a. F a. Industrial scale steam reforming of bioethanol: A conceptual study. Int J Hydrogen Energy 2010;35:8472–85. doi:10.1016/j.ijhydene.2010.05.003.

[64] Morgenstern DA, Fornango JP. Low-temperature reforming of ethanol over copper-plated raney nickel: A new route to sustainable hydrogen for transportation. Energy and Fuels 2005;19:1708–16. doi:10.1021/ef049692t.

[65] Vaidya PD, Rodrigues AE. Insight into steam reforming of ethanol to produce hydrogen for fuel cells. Chem Eng J 2006;117:39–49. doi:10.1016/j.cej.2005.12.008.

[66] Le Valant A, Can F, Bion N, Duprez D, Epron F. Hydrogen production from raw bioethanol steam reforming: Optimization of catalyst composition with improved stability against various impurities. Int J Hydrogen Energy 2010;35:5015–20. doi:10.1016/j.ijhydene.2009.09.008.

[67] Rostrup-Nielsen J. Catalytic Steam Reforming. vol. 5. 1984. doi:10.1007/978-3-642-93247-2_1.

[68] Rostrup-Nielsen JR, Sehested J. Hydrogen and Synthesis Gas by Steam- and CO * Reforming. Adv Catal 2002;47:65–139.

[69] Rossetti I, Sordelli L, Ghigna P, Pin S, Scavini M, Forni L. EXAFS-XANES evidence of in situ cesium reduction in Cs-Ru/C catalysts for ammonia synthesis. Inorg Chem 2011;50:3757–65. doi:10.1021/ic2001656.

[70] Rossetti I, Mangiarini F, Forni L. Promoters state and catalyst activation during ammonia synthesis over Ru/C. Appl Catal A Gen 2007;323:219–25.

[71] Rossetti I, Pernicone N, Forni L. Promoters effect in Ru/C ammonia synthesis catalyst. Appl Catal A Gen 2001;208:271–8.

[72] Bellido JD a, De Souza JE, M'Peko JC, Assaf EM. Effect of adding CaO to ZrO2 support on nickel catalyst activity in dry reforming of methane. Appl Catal A Gen 2009;358:215–23. doi:10.1016/j.apcata.2009.02.014.

[73] Rostrup-Nielsen JR. New aspects of syngas production and use. Catal Today 2000;63:159–64.

[74] Rossetti I, Lasso J, Nichele V, Signoretto M, Finocchio E, Ramis G, et al. Silica and zirconia supported catalysts for the low-temperature ethanol steam reforming. Appl Catal B Environ 2014;150–151:257–67. doi:10.1016/j.apcatb.2013.12.012.

[75] Compagnoni M, Lasso J, Di Michele A, Rossetti I. Flame pyrolysis prepared catalysts for the steam reforming of ethanol. Catal Sci Technol 2016:in press. doi:10.1039/C5CY01958C.

[76] Rossetti I, Compagnoni M, Torli M. Process simulation and optimisation of H2 production from ethanol steam reforming and its use in fuel cells. 1. Thermodynamic and kinetic analysis. Chem Eng J 2015;281:1024–35. doi:10.1016/j.cej.2015.08.025.

[77] Rossetti I, Compagnoni M, Torli M. Process simulation and optimization of H2 production from ethanol steam reforming and its use in fuel cells. 2. Process analysis and optimization. Chem Eng J 2015;281:1036–44. doi:10.1016/j.cej.2015.08.045.

[78] Rossetti I, Compagnoni M, Finocchio E, Ramis G, Di Michele A, Zucchini A, et al. Syngas production via steam reforming of bioethanol over Ni–BEA catalysts: A BTL strategy. Int J Hydrogen Energy 2016;41:16878–89. doi:http://dx.doi.org/10.1016/j.ijhydene.2016.07.149.

[79] Comazzi A, Pirola C, Di Michele A, Compagnoni M, Galli F, Rossetti I, et al. Flame Spray

Pyrolysis as fine preparation technique for stable Co and Co/Ru based catalysts for FT process. Appl Catal A Gen 2016;520:92–8. doi:10.1016/j.apcata.2016.04.010.

[80] Galetti AE, Gomez MF, Arrúa L a., Abello MC. Hydrogen production by ethanol reforming over NiZnAl catalysts. Influence of Ce addition on carbon deposition. Appl Catal A Gen 2008;348:94–102. doi:10.1016/j.apcata.2008.06.039.

[81] Nagase K, Shimodaira T, Itoh M, Zheng Y. Kinetics and mechanisms of the reverse Boudouard reaction over metal carbonates in connection with the reactions of solid carbon with the metal carbonates. Phys Chem Chem Phys 1999;1:5659–64. doi:10.1039/a906687j.

[82] Prasongthum N, Xiao R, Zhang H, Tsubaki N. Highly active and stable Ni supported on CNTs-SiO 2 fi ber catalysts for steam reforming of ethanol. Fuel Process Technol 2017;160:185–95. doi:10.1016/j.fuproc.2017.02.036.

[83] Palma V, Ruocco C, Meloni E, Gallucci F, Ricca A. Enhancing Pt-Ni/CeO2 performances for ethanol reforming by catalyst supporting on high surface silica. Catal Today 2016:in press. doi:10.1016/j.cattod.2017.05.034.

[84] Choong C, Zhong Z, Huang L, Borgna A, Hong L, Chen L, et al. Infrared evidence of a formate-intermediate mechanism over Ca-modified supports in low-temperature ethanol steam reforming. ACS Catal 2014;4:2359–63. doi:10.1021/cs500358n.

[85] Karim AM, Su Y, Sun J, Yang C, Strohm JJ, King DL, et al. A comparative study between Co and Rh for steam reforming of ethanol. Appl Catal B Environ 2010;96:441–8. doi:10.1016/j.apcatb.2010.02.041.

[86] Compagnoni M, Tripodi A, Rossetti I. Parametric study and kinetic testing for ethanol steam reforming. Appl Catal B Environ 2016;203:899–909. doi:10.1016/j.apcatb.2016.11.002.

[87] Tripodi A, Compagnoni M, Rossetti I. Kinetic modeling and reactor simulation for ethanol steam reforming. ChemCatChem 2016:1–11. doi:10.1002/cctc.201601075.

[88] Moraes TS, Rabelo Neto RC, Ribeiro MC, Mattos LV, Kourtelesis M, Ladas S, et al. Ethanol conversion at low temperature over CeO<inf>2</inf>-Supported Ni-based catalysts. Effect of Pt addition to Ni catalyst. Appl Catal B Environ 2016;181:754–68. doi:10.1016/j.apcatb.2015.08.044.

[89] Díaz Alvarado F, Gracia F. Steam reforming of ethanol for hydrogen production: Thermodynamic analysis including different carbon deposits representation. Chem Eng J 2010;165:649–57. doi:10.1016/j.cej.2010.09.051.

[90] Trimm DL. Coke formation and minimisation during steam reforming reactions. Catal Today 1997;37:233–8. doi:10.1016/S0920-5861(97)00014-X.

[91] Donazzi A, Pagani D, Lucotti A, Tommasini M, Beretta A, Groppi G, et al. Annular reactor testing and Raman surface characterization in the CPO of methane and propylene. Appl Catal A Gen 2014;474:149–58. doi:10.1016/j.apcata.2013.06.005.

[92] Serrano-Lotina a., Daza L. Long-term stability test of Ni-based catalyst in carbon dioxide reforming of methane. Appl Catal A Gen 2014;474:107–13. doi:10.1016/j.apcata.2013.08.027.

[93] McFarland EW, Metiu H. Catalysis by doped oxides. Chem Rev 2013;113:4391–427. doi:10.1021/cr300418s.

[94] Nichele V, Signoretto M, Pinna F, Ghedini E, Compagnoni M, Rossetti I, et al. Bimetallic Ni–Cu Catalysts for the Low-Temperature Ethanol Steam Reforming: Importance of Metal–Support Interactions. Catal Letters 2014;145:549–58. doi:10.1007/s10562-014-1414-2.

[95] Compagnoni M, Kondrat SA, Chan-Thaw CE, Morgan DJ, Wang D, Prati L, et al.

Spectroscopic Investigation of Titania-Supported Gold Nanoparticles Prepared by a Modified Deposition/Precipitation Method for the Oxidation of CO. ChemCatChem 2016;8:2136–45. doi:10.1002/cctc.201600072.

[96] Mädler L, Roessler a., Pratsinis SE, Sahm T, Gurlo a., Barsan N, et al. Direct formation of highly porous gas-sensing films by in situ thermophoretic deposition of flame-made Pt/SnO2 nanoparticles. Sensors Actuators B Chem 2006;114:283–95. doi:10.1016/j.snb.2005.05.014.

Tables

Table 1

Textural and morphological properties of the FP prepared catalysts. S_{BET} = BET specific surface area; V_p = pore volume; d_p = mean pore diameter; d_{ZrO2} = ZrO_2 crystal size from XRD; d_{Ni} = NiO crystal size from XRD. [a] obtained by N_2 physisorption; [b] obtained by Sherrer equation; [c] obtained by TPR.

Catalyst	Composition (wt%)			S_{BET} [a] (m^2 g^{-1})	V_p [a] (cm^3 g^{-1})	d_p [a] (nm)	d_{ZrO2} [b] (nm)	d_{Ni} [b] (nm)	mol H_2 consumed / mol Ni [c]
Zr-Ni	Ni - 10	-	ZrO_2	53	0.21	1.00	22	12	1.00
CaZr-Ni	Ni - 10	CaO - 4	ZrO_2	49	0.17	1.00	23	10	1.00
MgZr-Ni	Ni - 10	MgO - 4	ZrO_2	49	0.15	0.45	20	11	0.45
KZr-Ni	Ni - 10	K_2O - 4	ZrO_2	25	0.11	0.96	35	16	0.96
KZr-Ni PI	Ni - 10	K_2O - 9	ZrO_2	55	-	1.00	-	-	-

Table 2

Activity testing for LT-ESR at 500°C and 400°C, 8h time-on-stream, data averaged out at 4-8 h-on-stream, GHSV = 2700 h^{-1}, Steam/Ethanol = 3 mol/mol.

Catalysts	Zr-Ni	CaZr-Ni	MgZr-Ni	KZr-Ni	Equilibrium
500°C					
EtOH conversion (%)	100 ± 0	100 ± 0	100 ± 0	100 ± 0	100
H_2 productivity (mol min^{-1} kg_{cat}^{-1})	1.04 ± 0.03	1.07 ± 0.10	1.04 ± 0.08	1.16 ± 0.10	1.23
CO/CO_2	0.82 ± 0.14	0.64 ± 0.10	1.13 ± 0.11	0.74 ± 0.04	0.601
C balance (%)	81 ± 3	89 ± 4	83 ± 7	87 ± 2	-
Sel. CH_4 (%)	10.7 ± 1.5	19 ± 2	9.4 ± 1.1	3.97 ± 0.10	33.4
Sel. CH_3CHO (%)	0 ± 0	0 ± 0	0 ± 0	0 ± 0	$1.1\ 10^{-8}$
Sel. CH_2CH_2 (%)	0 ± 0	0 ± 0	0.9 ± 0.9	0 ± 0	$2.2\ 10^{-6}$
400°C					
EtOH conversion (%)	100 ± 0	100 ± 0	53 ± 9	100 ± 0	100
H_2 productivity (mol min^{-1} kg_{cat}^{-1})	0.65 ± 0.04	0.752 ± 0.006	0.23 ± 0.02	1.00 ± 0.05	0.675
CO/CO_2	1.2 ± 0.2	0.2 ± 0.2	1.15 ± 0.08	0.242 ± 0.006	0.093
C balance (%)	56 ± 4	87 ± 4	86 ± 11	84.2 ± 0.7	-
Sel. CH_4 (%)	16 ± 2	37 ± 3	9 ± 2	16.7 ± 0.4	92.1
Sel. CH_3CHO (%)	0 ± 0	0 ± 0	30 ± 4	0 ± 0	$3.3\ 10^{-9}$
Sel. CH_2CH_2 (%)	0 ± 0	0 ± 0	7 ± 1	0 ± 0	$4.0\ 10^{-7}$

Table 3

Activity testing for LT-ESR at 500 °C and 400°C, 8h time-on-stream, data averaged out at 4-8 h-on-stream, GHSV = 2700 h^{-1}, Steam/Ethanol = 3 mol/mol, different preparation methods (PI = Precipitation-Impregnation).

Catalysts	CaZr-Ni	CaZr-Ni PI	KZr-Ni	KZr-Ni PI
500°C				
EtOH conversion (%)	100 ± 0	100 ± 0	100 ± 0	100 ± 0
Sel. CH_4 (%)	19 ± 2	13 ± 1	3.97 ± 0.10	10.0 ± 0.4
Sel. CH_3CHO (%)	0 ± 0	2.2 ± 0.4	0 ± 0	0 ± 0
Sel. CH_2CH_2 (%)	0 ± 0	0 ± 0	0 ± 0	0 ± 0
CO/CO_2	0.64 ± 0.10	0.44 ± 0.07	0.74 ± 0.04	0.96 ± 0.08
H_2 productivity (mol min^{-1} kg_{cat}^{-1})	1.07 ± 0.10	0.86 ± 0.05	1.16 ± 0.10	1.15 ± 0.05
400°C				
EtOH conversion (%)	100 ± 0	62 ± 9 (decreasing)	100 ± 0	100 ± 0
Sel. CH_4 (%)	37 ± 3	2.1 ± 0.5	16.7 ± 0.4	10.0 ± 0.4
Sel. CH_3CHO (%)	0 ± 0	7 ± 2	0 ± 0	0 ± 0
Sel. CH_2CH_2 (%)	0 ± 0	20 ± 5 (increasing)	0 ± 0	0 ± 0
CO/CO_2	0.2 ± 0.2	0.28 ± 0.03	0.242 ± 0.006	0.21 ± 0.02
H_2 productivity (mol min^{-1} kg_{cat}^{-1})	0.752 ± 0.006	0.3 ± 0.4	1.00 ± 0.05	0.96 ± 0.04

Figures

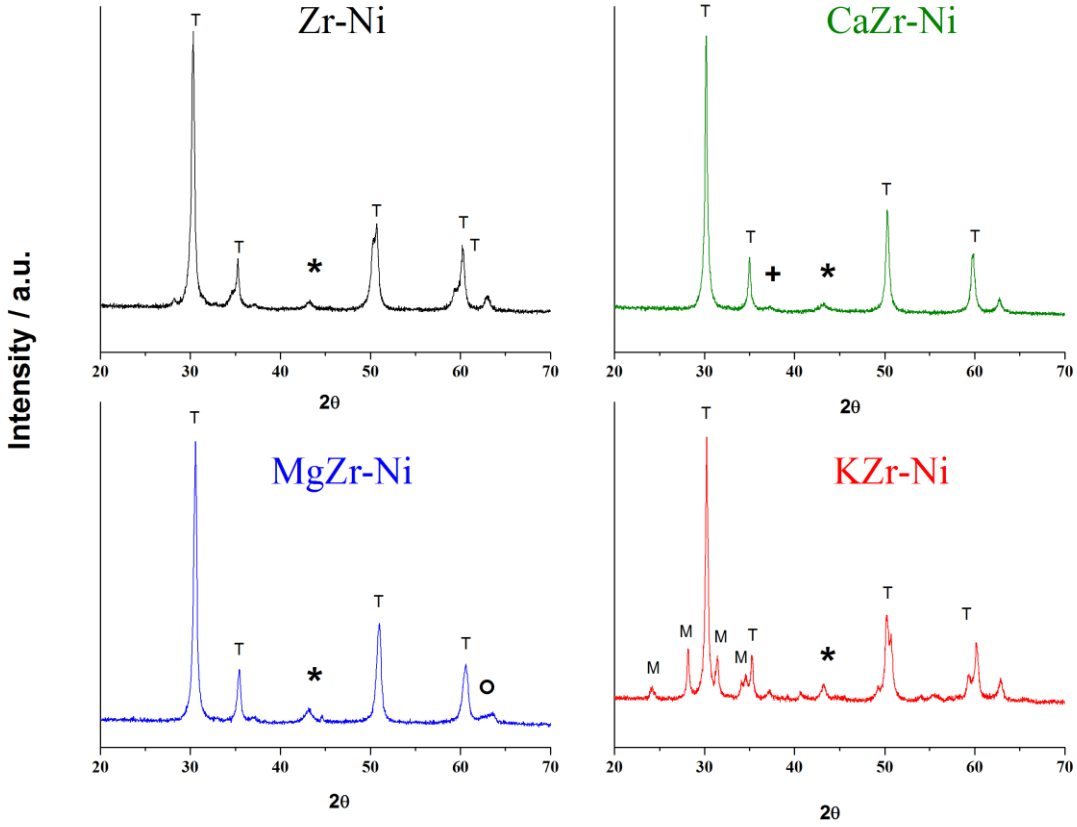

Fig. 1 XRD patterns of catalysts with various dopants: (*) nickel oxide, (+) calcium oxide, (°) magnesium oxide, (T) tetragonal phase, (M) monoclinic phase of zirconia.

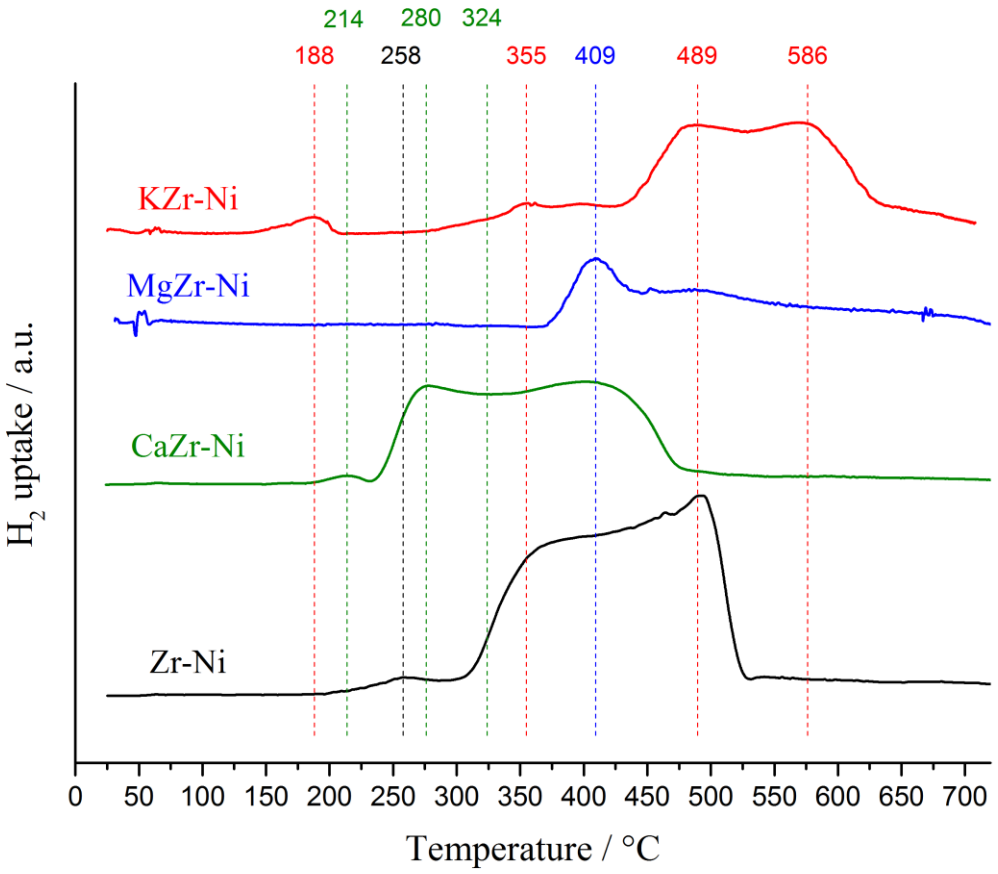

Fig. 2 H_2-TPR profiles of the FSP catalysts prepared with different basic promoters. Peaks deconvolution is reported in Fig. S2 and S3.

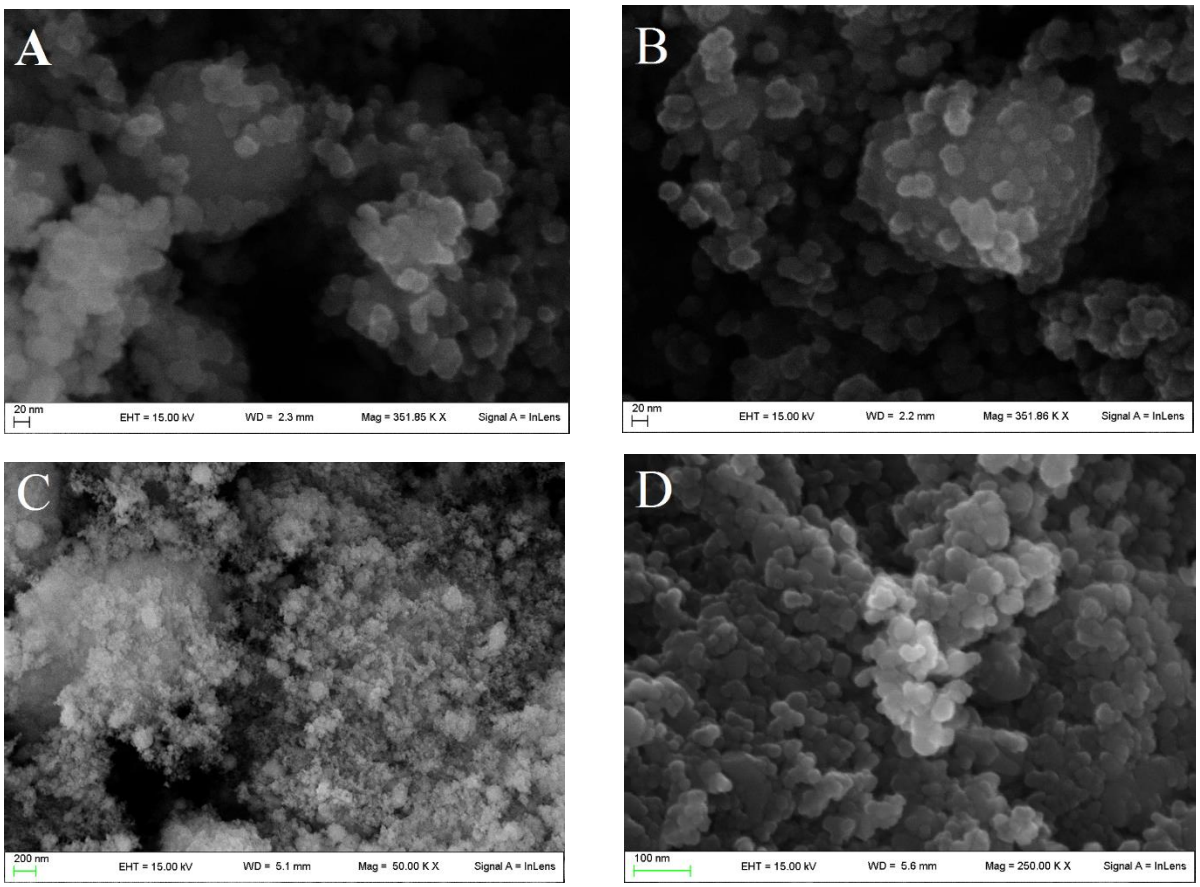

Fig. 3 FE-SEM images of Ni/M_xO-ZrO_2 synthesised by FSP; A) Zr-Ni; B) CaZr-Ni; C) MgZr-Ni; D) KZr-Ni. Marker size 20nm for A) and B), 200nm for C) and 100nm for D).

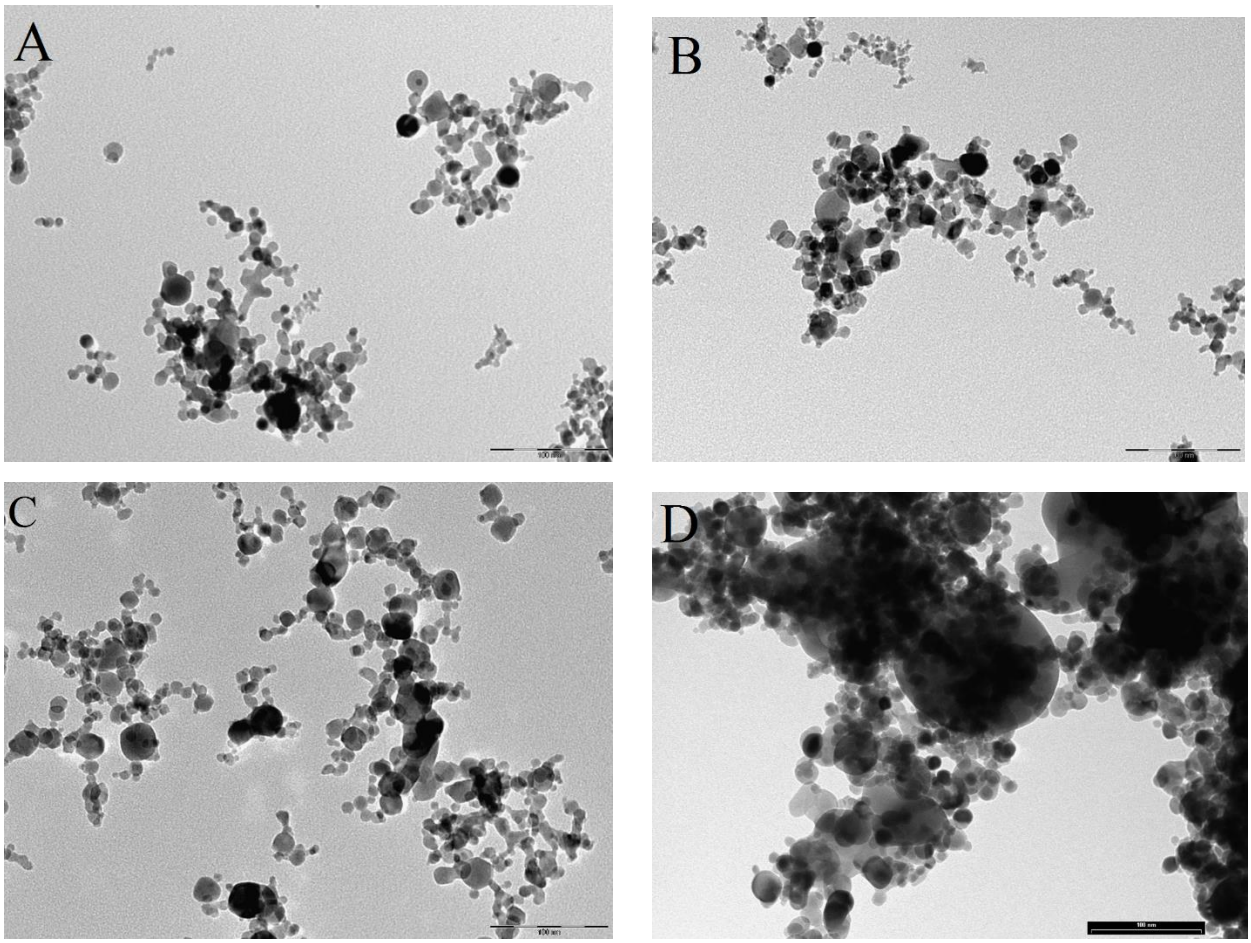

Fig. 4 TEM images of Ni/M_xO-ZrO_2 synthesised by FSP; A) Zr-Ni; B) CaZr-Ni; C) MgZr-Ni; D) KZr-Ni. Marker size 100nm. Darker dots are attributed to Ni/NiO particles.

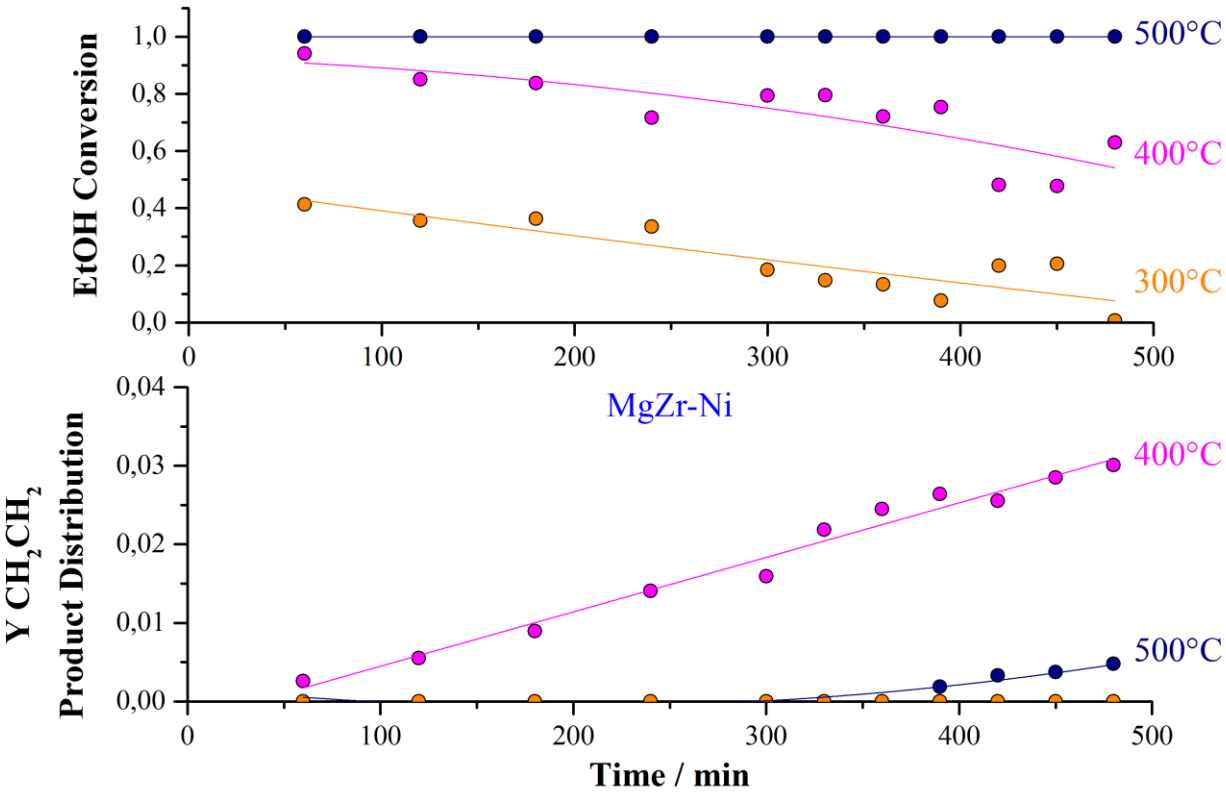

Fig. 5 Evolution with time-on-stream of ethanol conversion (upper) and ethylene production (lower) for MgZr-Ni at different temperature.

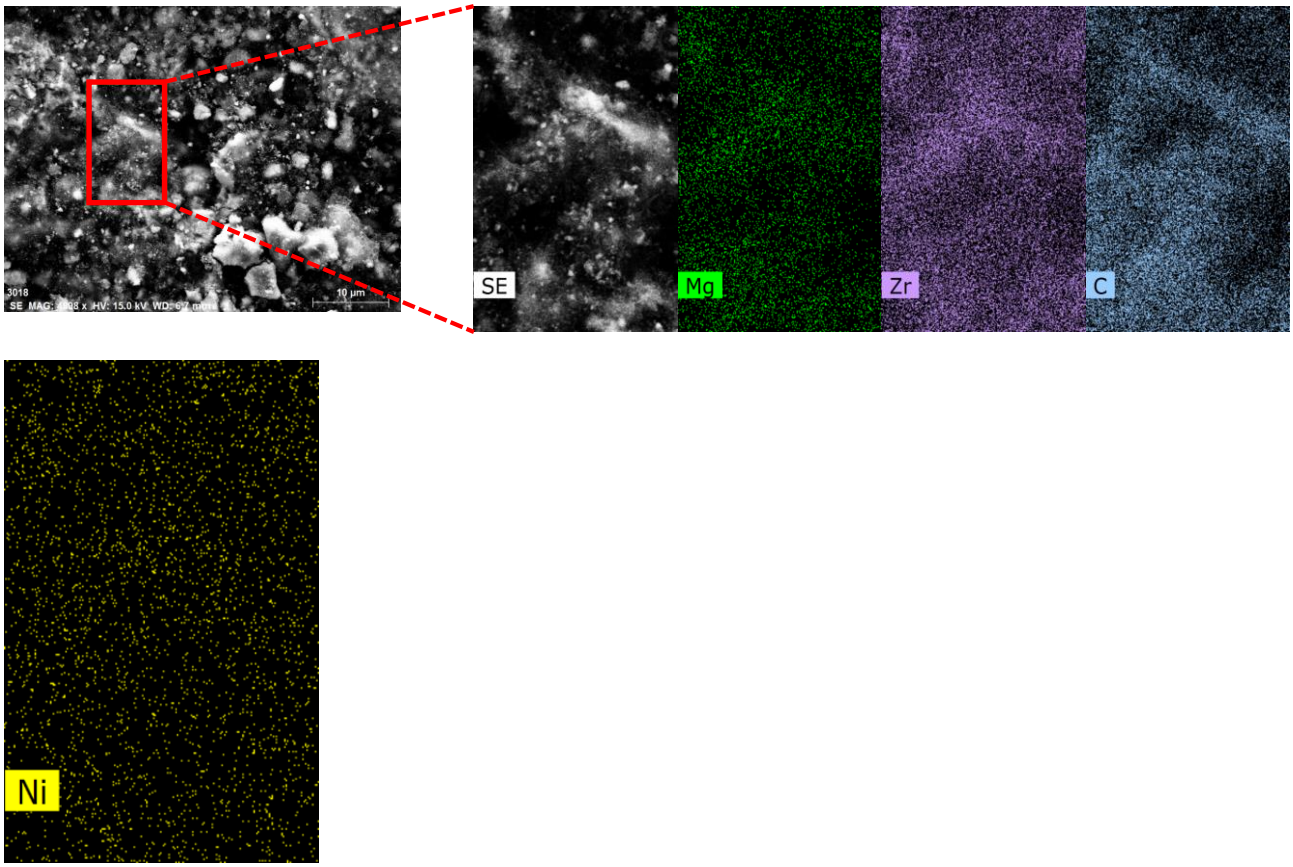

Fig 6 Representative elemental mapping images by EDX-SEM of Mg for spent MgZr-Ni

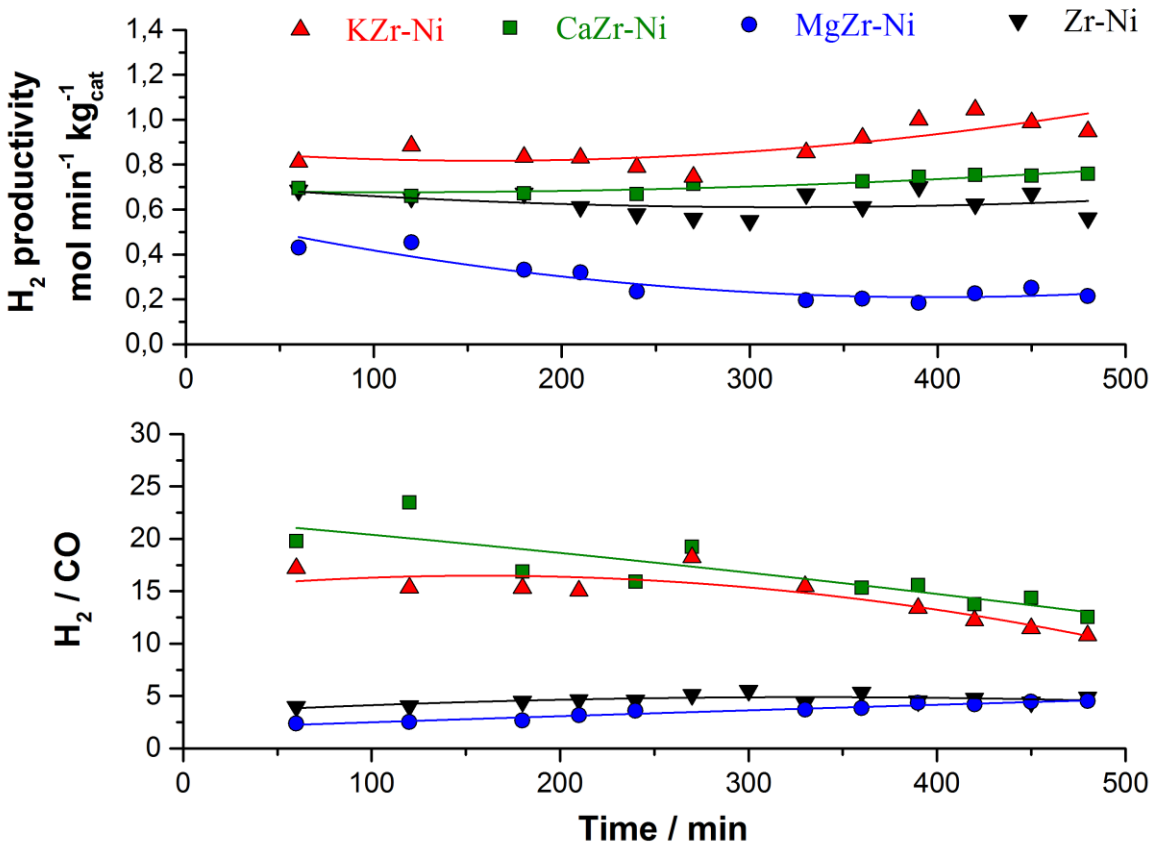

Fig. 7 H_2 productivity and H_2/CO ratio versus time on stream at 400 °C: S/E = 3 mol/mol; GHSV = 2700 h^{-1}; P = 1 atm.

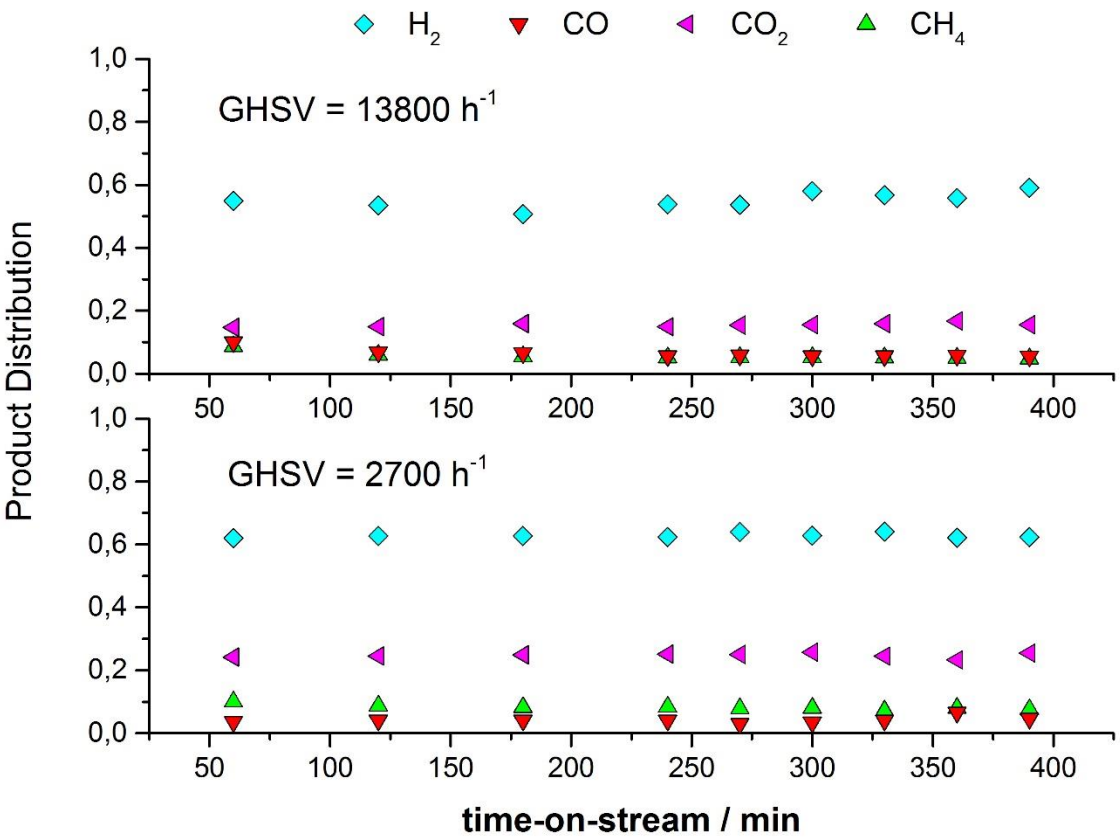

Fig. 8 Products distribution of sample KZr-Ni considering test with a tenth of catalyst mass with respect to standard testing conditions (GHSV = 13800 h^{-1}, T = 400 °C, S/E = 3 mol/mol, P = 1 atm, Average ethanol conversion = 42 ± 4 %)

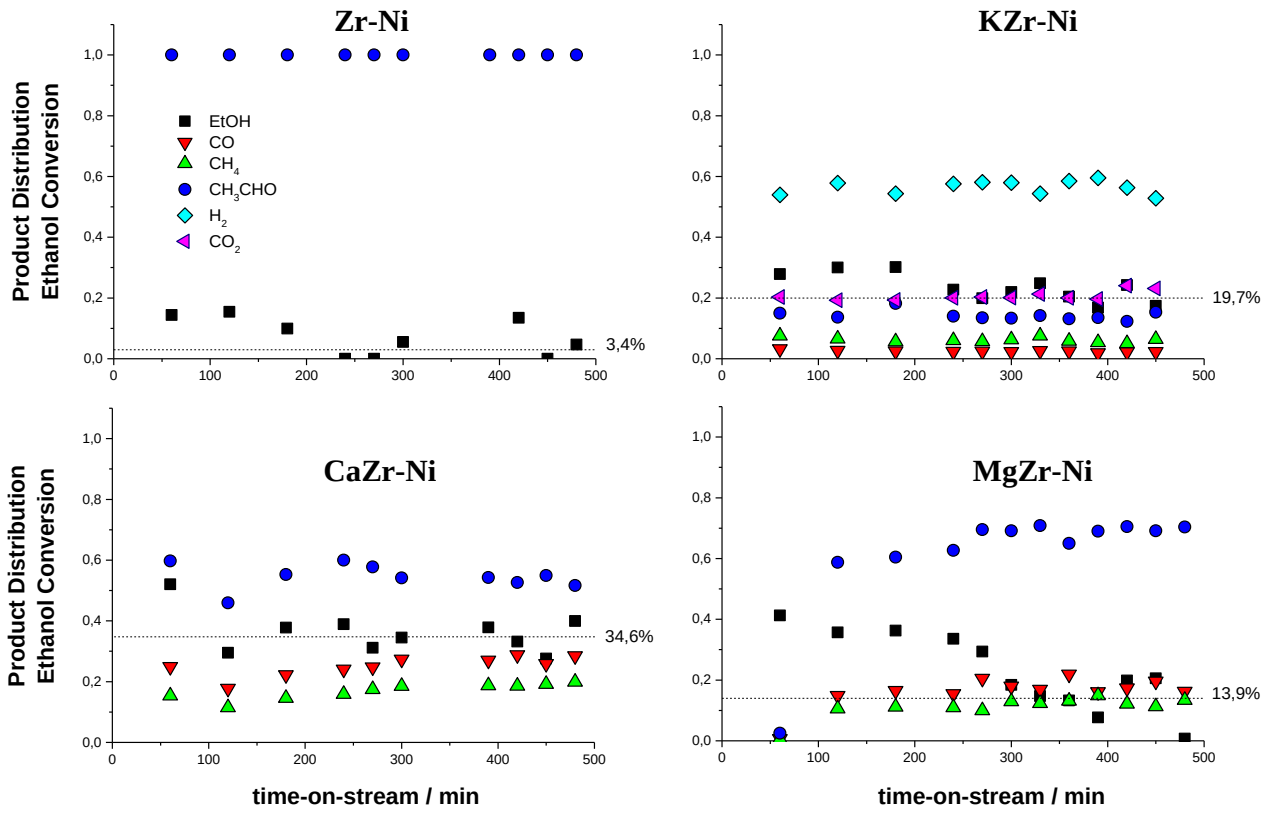

Fig. 9 Products distribution and ethanol conversion for LT-ESR tests at 300 °C, S/E = 3 mol/mol; GHSV = 2700 h^{-1}; P = 1 atm.

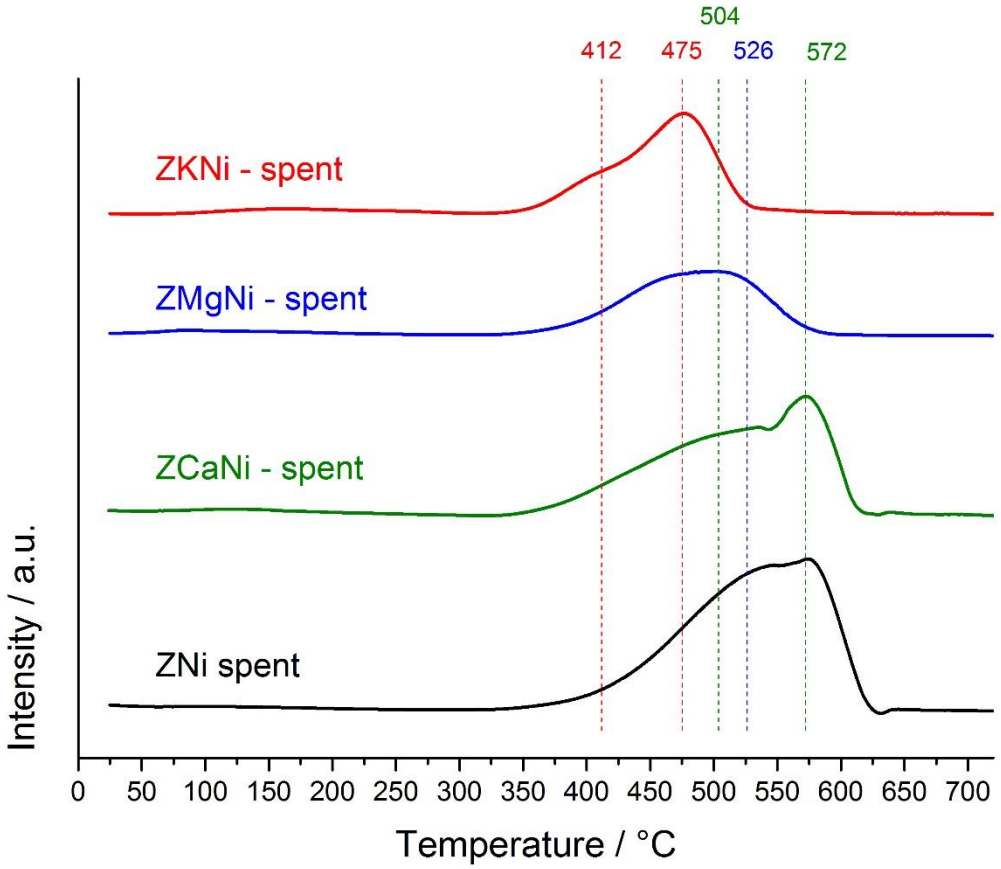

Fig. 10 TPO profiles of the catalysts after the LT-ESR the full testing sequence at 500, 400 and 300 °C.

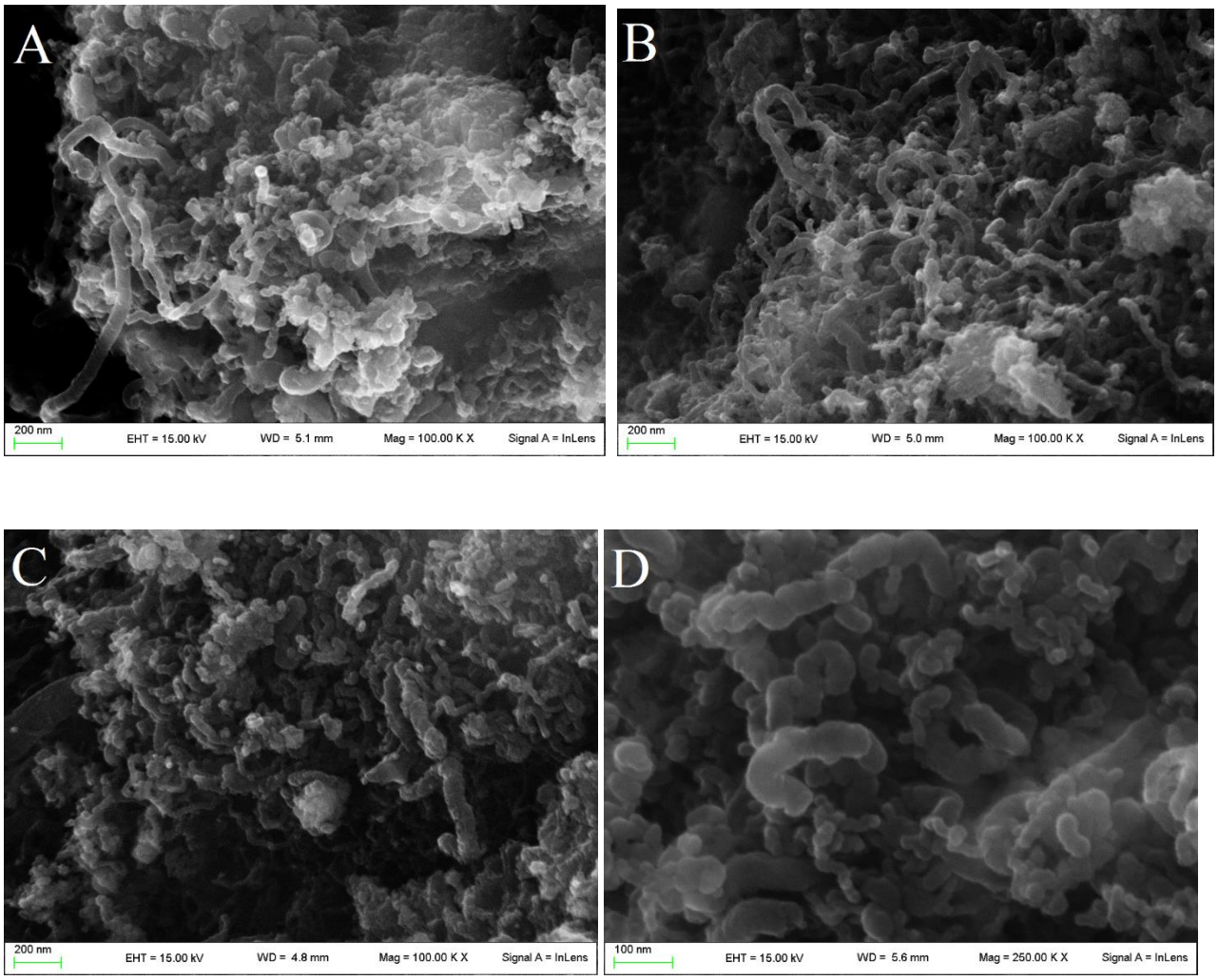

Fig. 11 FE-SEM micrographs of catalysts after the LT-ESR tests: A) Zr-Ni; B) CaZr-Ni; C) MgZr-Ni; D) KZr-Ni. Marker size 200nm for A), B), C), and 100nm for D).

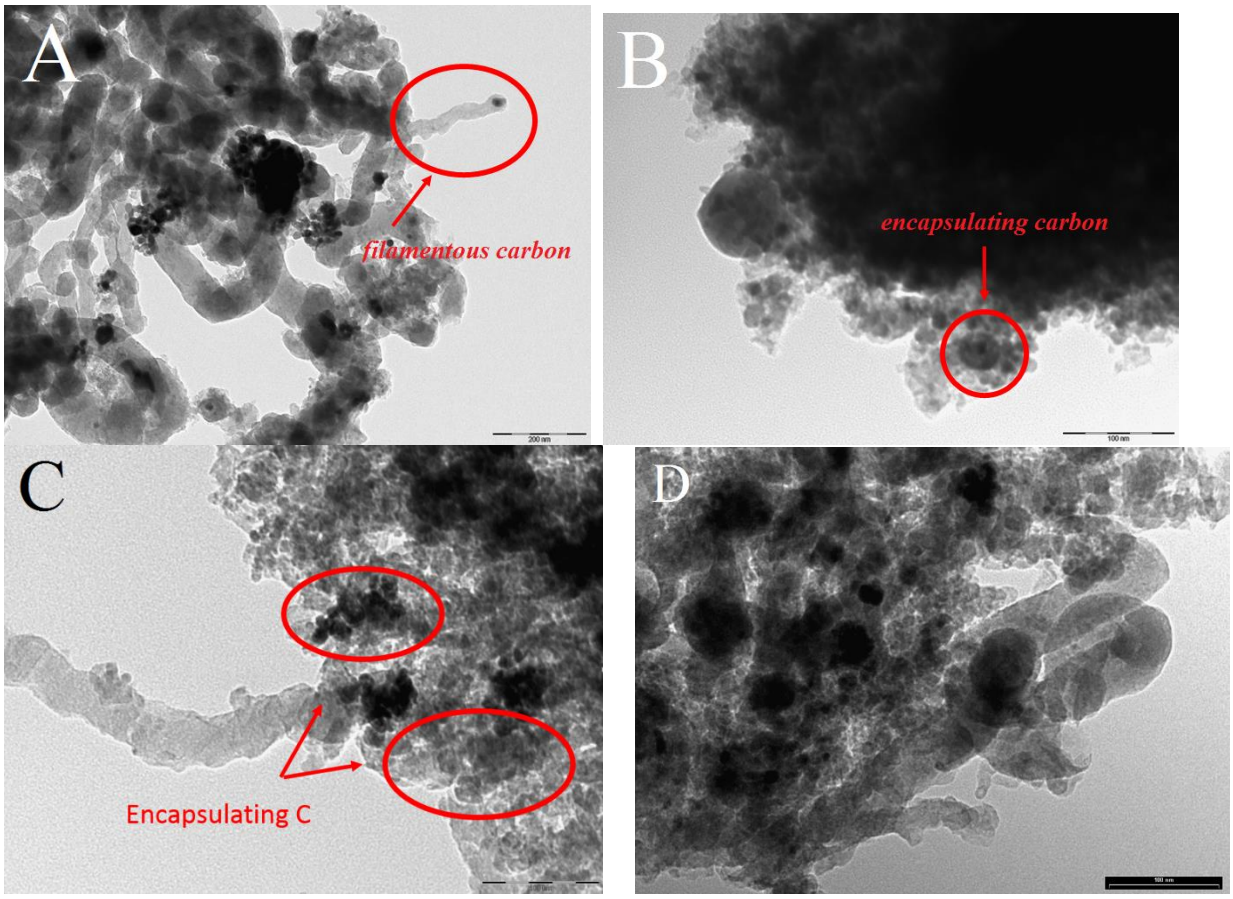

Fig. 12 TEM micrographs of catalysts after the LT-ESR tests: A) Zr-Ni; B) CaZr-Ni; C) MgZr-Ni; D) KZr-Ni. Marker size 200nm for A), 500nm for C), and 100nm for B) and D).

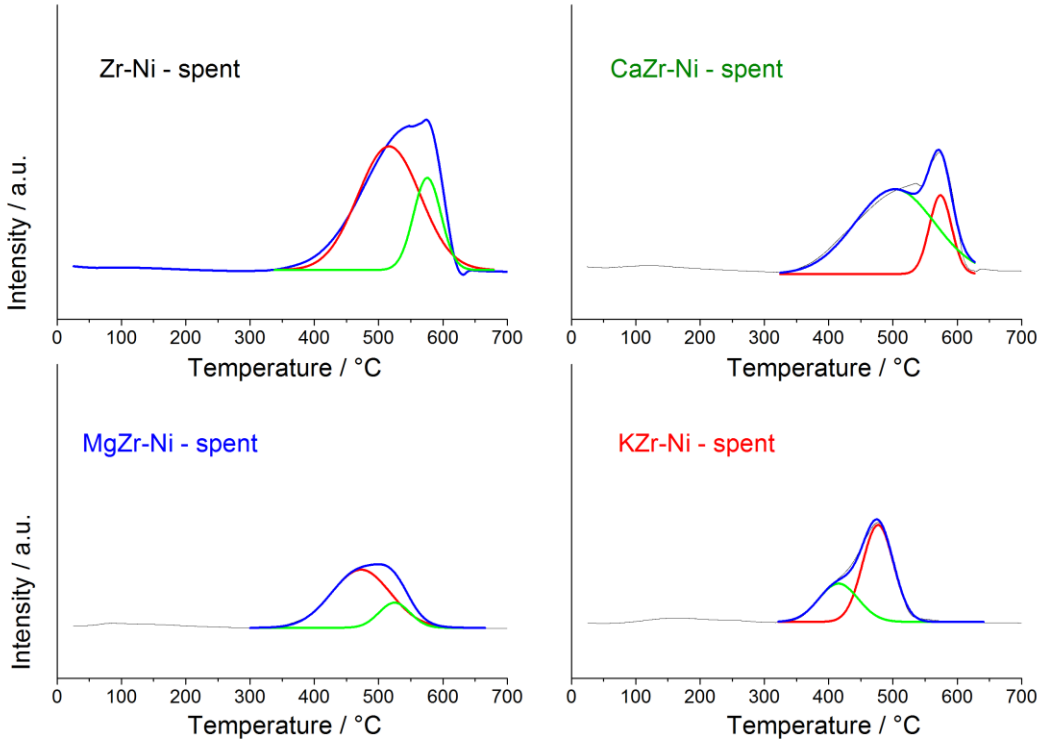

Fig. 13 TPO profiles deconvolution of the catalysts after the LT-ESR testing.

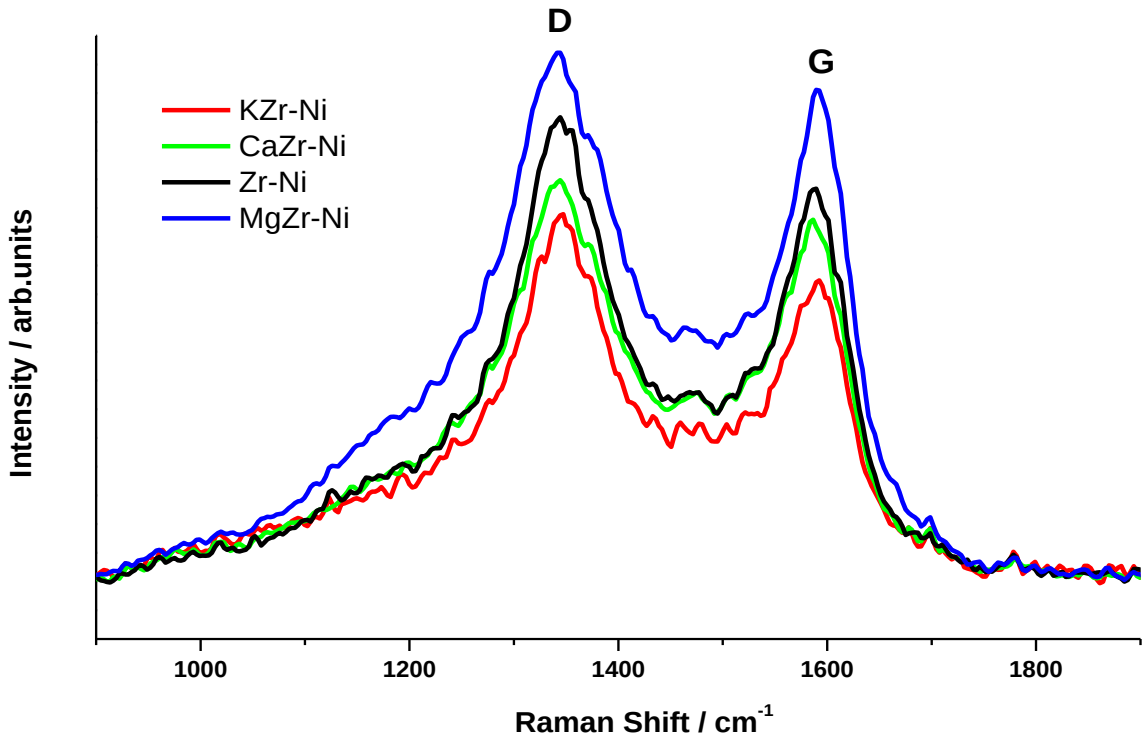

Fig. 14 Raman spectra of the spent samples. From bottom up: KZr-Ni, CaZr-Ni, Zr-Ni, MgZr-Ni

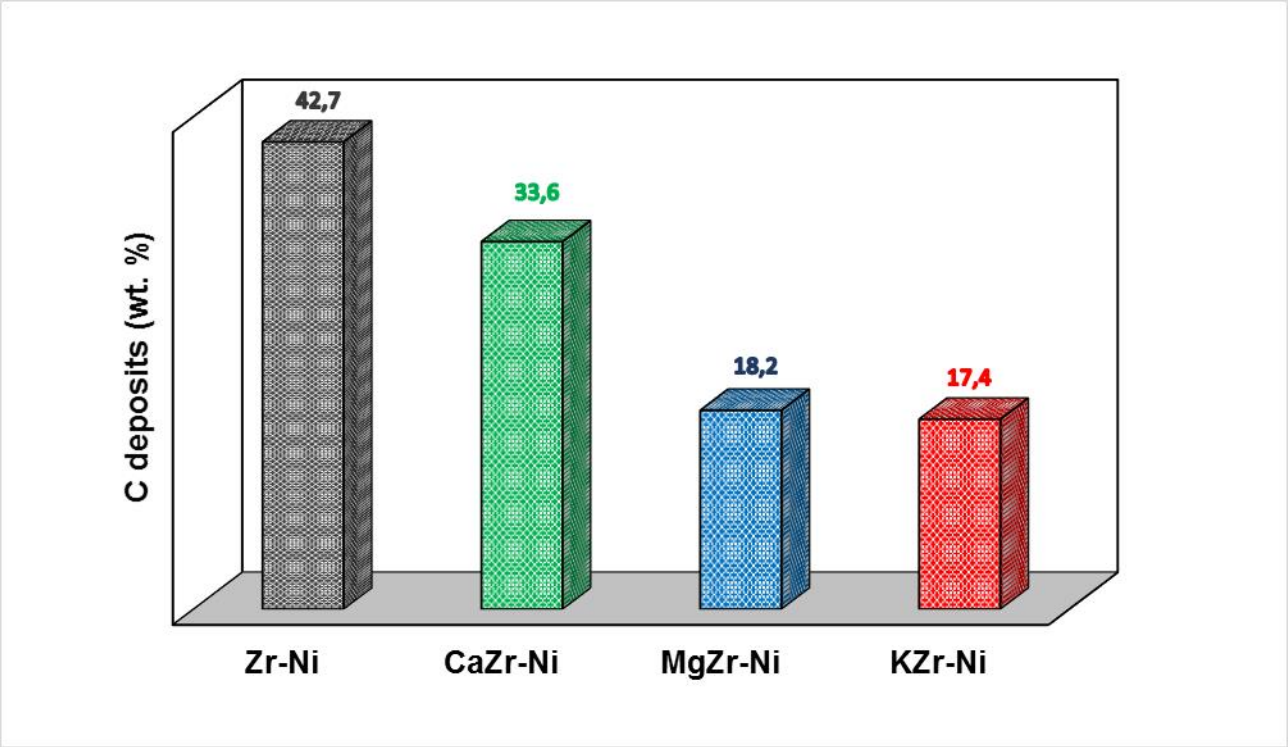

Fig. 15 Coke accumulated over Ni-based catalysts used in the LT-ESR (temperature sequence: 500, 400, 300 °C) from TPO analysis.